CHAPTER 14

MICROSTRIP ANTENNAS

14.1 INTRODUCTION

In high-performance aircraft, spacecraft, satellite and missile applications, where size, weight, cost, performance, ease of installation, and aerodynamic profile are constraints, low profile antennas may be required. Presently there are many other government and commercial applications, such as mobile radio and wireless communications, that have similar specifications. To meet these requirements, microstrip antennas [1]–[38] can be used. These antennas are low-profile, conformable to planar and nonplanar surfaces, simple and inexpensive to manufacture using modern printed-circuit technology, mechanically robust when mounted on rigid surfaces, compatible with MMIC designs, and when the particular patch shape and mode are selected they are very versatile in terms of resonant frequency, polarization, pattern and impedance. In addition, by adding loads between the patch and the ground plane, such as pins and varactor diodes, adaptive elements with variable resonant frequency, impedance, polarization and pattern can be designed [18], [39]–[44].

Major operational disadvantages of microstrip antennas are their low efficiency, low power, high Q (sometimes in excess of 100), poor polarization purity, poor scan performance, spurious feed radiation and very narrow frequency bandwidth, which is typically only a fraction of a percent or at most a few percent. In some applications, such as in government security systems, narrow bandwidths are desirable. However, there are methods, such by increasing the height of the substrate, that can be used to extend the efficiency (as large as 90 percent if surface waves are not included) and bandwidth (up to about 35 percent) [38]. However, as the height increases, surface waves are introduced which usually are not desirable because they extract power from the total available for direct radiation (space waves). The surface waves travel within the substrate and they are scattered at bends and surface discontinuities, such as the truncation of the dielectric and ground plane [45]–[49], and degrade the antenna pattern and polarization characteristics. Surface waves can be eliminated, while maintaining large bandwidths, by using cavities [50], [51]. Stacking, as well as other methods, of microstrip elements can also be used to increase the bandwidth [13], [52]–[62]. In addition, microstrip antennas also exhibit large electromagnetic signature at certain frequencies outside the operating band, are rather large physically at VHF and possibly UHF frequencies, and in large arrays there is a tradeoff between bandwidth and scan volume [63]–[65].

14.1.1 Basic Characteristics

Microstrip antennas received considerable attention starting in the 1970s, although the idea of a microstrip antenna can be traced to 1953 [1] and a patent in 1955 [2]. Microstrip antennas, as shown in Figure 14.1(a), consist of a very thin ($t \ll \lambda_0$ where λ_0 is the free-space wavelength) metallic strip (patch) placed a small fraction of a wavelength ($h \ll \lambda_0$, usually $0.003\lambda_0 \leq h \leq 0.05\lambda_0$) above a ground plane. The microstrip patch is designed so its pattern maximum is normal to the patch (broadside radiator). This is accomplished by properly choosing the mode (field configuration) of excitation beneath the patch. End-fire radiation can also be accomplished by judicious mode selection. For a rectangular patch, the length L of the element is usually $\lambda_0/3 < L < \lambda_0/2$. The strip (patch) and the ground plane are separated by a dielectric sheet (referred to as the substrate), as shown in Figure 14.1(a).

There are numerous substrates that can be used for the design of microstrip antennas, and their dielectric constants are usually in the range of $2.2 \leq \epsilon_r \leq 12$. The ones that are most desirable for antenna performance are thick substrates whose dielectric constant is in the lower end of the range because they provide better efficiency, larger bandwidth, loosely bound fields for radiation into space, but at the expense of larger element size [38]. Thin substrates with higher dielectric constants are desirable for microwave circuitry because they require tightly bound fields to minimize undesired radiation and coupling, and lead to smaller element sizes; however, because of their greater losses, they are less efficient and have relatively smaller bandwidths [38]. Since microstrip antennas are often integrated with other microwave circuitry, a compromise has to be reached between good antenna performance and circuit design.

Often microstrip antennas are also referred to as *patch* antennas. The radiating elements and the feed lines are usually photoetched on the dielectric substrate. The radiating patch may be square, rectangular, thin strip (dipole), circular, elliptical, triangular or any other configuration. These and others are illustrated in Figure 14.2.

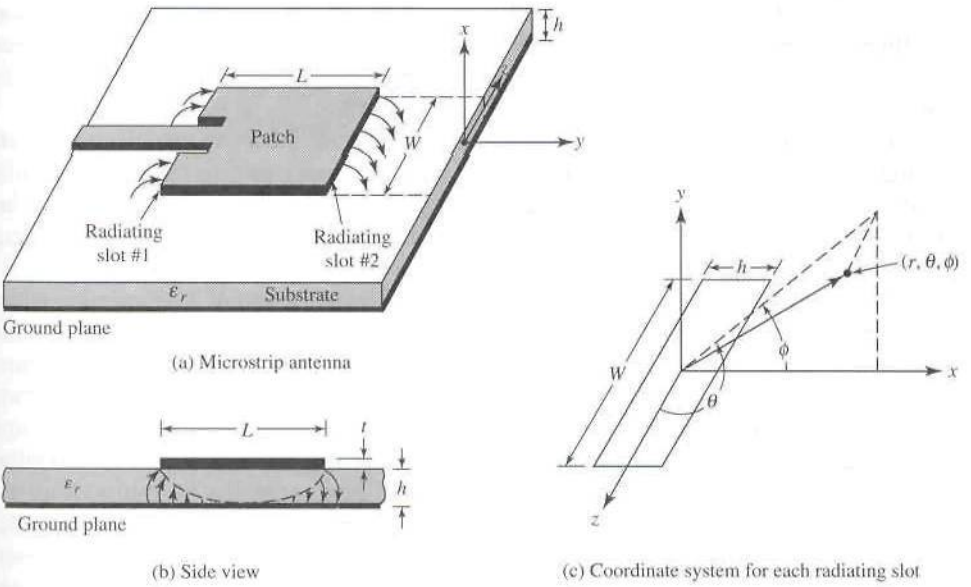

Figure 14.1 Microstrip antenna and coordinate system.

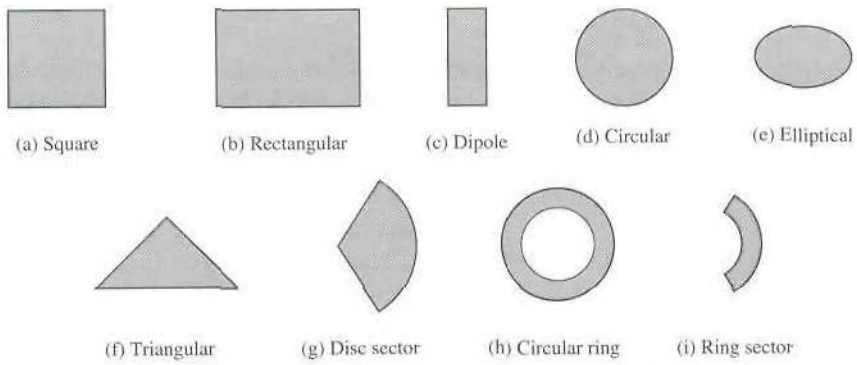

Figure 14.2 Representative shapes of microstrip patch elements.

Square, rectangular, dipole (strip), and circular are the most common because of ease of analysis and fabrication, and their attractive radiation characteristics, especially low cross-polarization radiation. Microstrip dipoles are attractive because they inherently possess a large bandwidth and occupy less space, which makes them attractive for arrays [14], [22], [30], [31]. Linear and circular polarizations can be achieved with either single elements or arrays of microstrip antennas. Arrays of microstrip elements, with single or multiple feeds, may also be used to introduce scanning capabilities and achieve greater directivities. These will be discussed in later sections.

14.1.2 Feeding Methods

There are many configurations that can be used to feed microstrip antennas. The four most popular are the microstrip line, coaxial probe, aperture coupling and proximity coupling [15], [16], [30], [35], [38], [66]–[68]. These are displayed in Figure 14.3. One set of equivalent circuits for each one of these is shown in Figure 14.4. The microstrip feed line is also a conducting strip, usually of much smaller width compared to the patch. The microstrip line feed is easy to fabricate, simple to match by controlling the inset position and rather simple to model. However as the substrate thickness increases surface waves and spurious feed radiation increase, which for practical designs limit the bandwidth (typically 2–5%).

Coaxial-line feeds, where the inner conductor of the coax is attached to the radiation patch while the outer conductor is connected to the ground plane, are also widely used. The coaxial probe feed is also easy to fabricate and match, and it has low spurious radiation. However, it also has narrow bandwidth and it is more difficult to model, especially for thick substrates ($h > 0.02\lambda_0$).

Both the microstrip feed line and the probe possess inherent asymmetries which generate higher order modes which produce cross-polarized radiation. To overcome some of these problems, noncontacting aperture coupling feeds, as shown in Figures 14.3(c,d), have been introduced. The aperture coupling of Figure 14.3(c) is the most difficult of all four to fabricate and it also has narrow bandwidth. However, it is somewhat easier to model and has moderate spurious radiation. The aperture coupling consists of two substrates separated by a ground plane. On the bottom side of the lower substrate there is a microstrip feed line whose energy is coupled to the patch through a slot on the ground plane separating the two substrates. This arrangement allows independent optimization of the feed mechanism and the radiating element. Typically a high dielectric material is used for the bottom substrate, and thick low

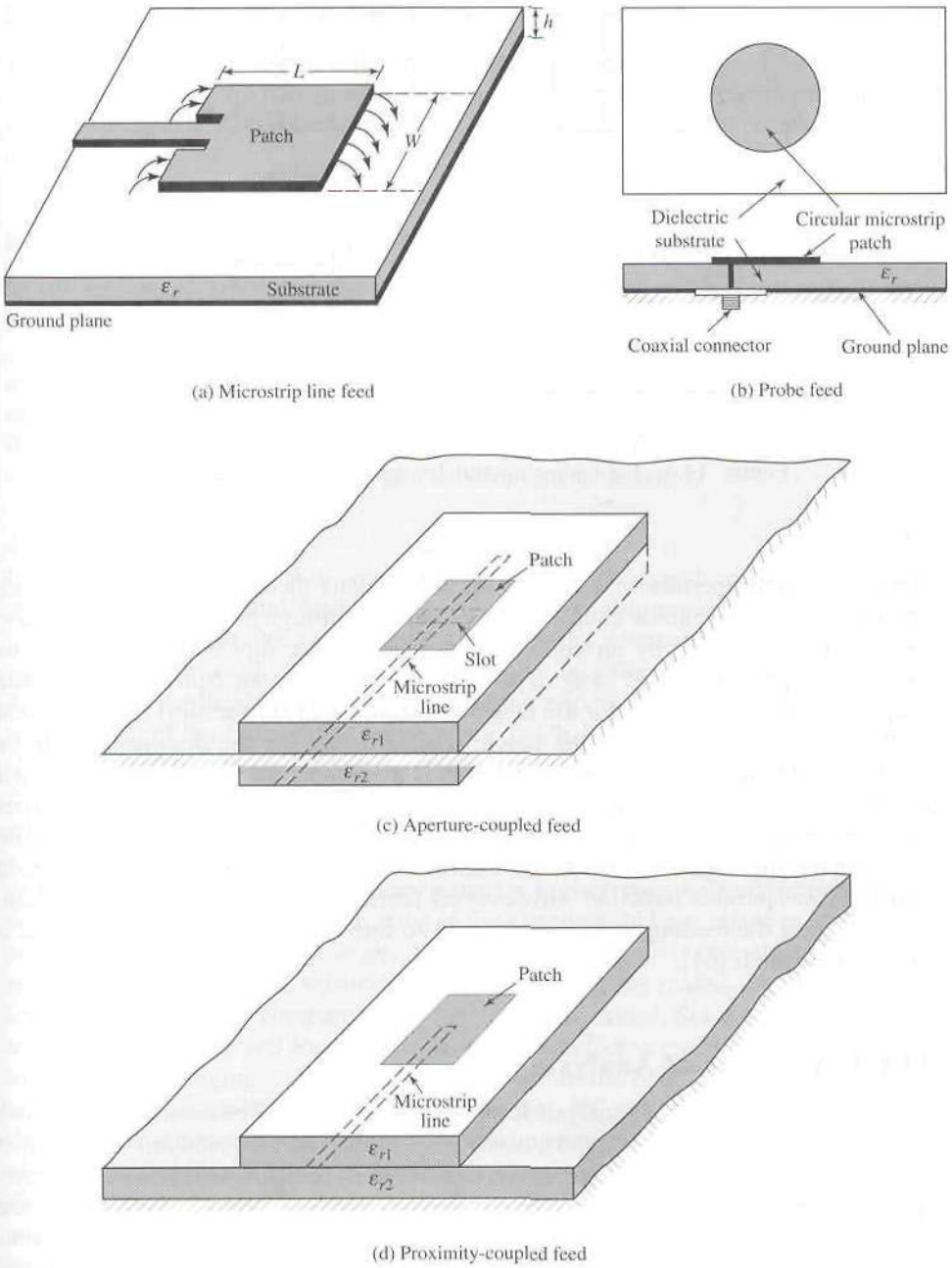

(a) Microstrip line feed

(b) Probe feed

(c) Aperture-coupled feed

(d) Proximity-coupled feed

Figure 14.3 Typical feeds for microstrip antennas.

dielectric constant material for the top substrate. The ground plane between the substrates also isolates the feed from the radiating element and minimizes interference of spurious radiation for pattern formation and polarization purity. For this design, the substrate electrical parameters, feed line width, and slot size and position can be used to optimize the design [38]. Typically matching is performed by controlling the width of the feed line and the length of the slot. The coupling through the slot can be modeled using the theory of Bethe [69], which is also used to account for coupling

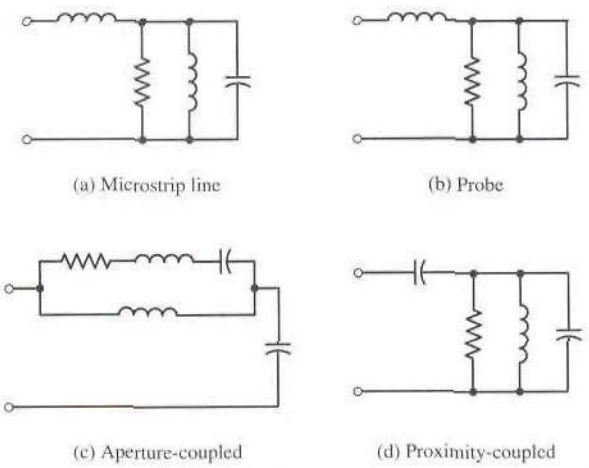

Figure 14.4 Equivalent circuits for typical feeds of Figure 14.3.

through a small aperture in a conducting plane. This theory has been successfully used to analyze waveguide couplers using coupling through holes [70]. In this theory the slot is represented by an equivalent normal electric dipole to account for the normal component (to the slot) of the electric field and an equivalent horizontal magnetic dipole to account for the tangential component (to the slot) magnetic field. If the slot is centered below the patch, where ideally for the dominant mode the electric field is zero while the magnetic field is maximum, the magnetic coupling will dominate. Doing this also leads to good polarization purity and no cross-polarized radiation in the principal planes [38]. Of the four feeds described here, the proximity coupling has the largest bandwidth (as high as 13 percent), is somewhat easy to model and has low spurious radiation. However its fabrication is somewhat more difficult. The length of the feeding stub and the width-to-line ratio of the patch can be used to control the match [61].

14.1.3. Methods of Analysis

There are many methods of analysis for microstrip antennas. The most popular models are the *transmission-line* [16], [35], *cavity* [12], [16], [18], [35], and *full-wave* (which include primarily integral equations/Moment Method) [22], [26], [71]–[74]. The transmission-line model is the easiest of all, it gives good physical insight, but is less accurate and it is more difficult to model coupling [75]. Compared to the transmission-line model, the cavity model is more accurate but at the same time more complex. However, it also gives good physical insight and is rather difficult to model coupling, although it has been used successfully [8], [76], [77]. In general when applied properly, the full-wave models are very accurate, very versatile, and can treat single elements, finite and infinite arrays, stacked elements, arbitrary shaped elements, and coupling. However they are the most complex models and usually give less physical insight. In this chapter we will cover the transmission-line and cavity models only. However results and design curves from full-wave models will also be included. Since they are the most popular and practical, in this chapter the only two patch configurations that will be considered are the rectangular and circular. Representative radiation characteristics of some other configurations will be included.

14.2 RECTANGULAR PATCH

The rectangular patch is by far the most widely used configuration. It is very easy to analyze using both the transmission-line and cavity models, which are most accurate for thin substrates [78]. We begin with the transmission-line model because it is easier to illustrate.

14.2.1 Transmission-Line Model

It was indicated earlier that the transmission-line model is the easiest of all but it yields the least accurate results and it lacks the versatility. However, it does shed some physical insight. As it will be demonstrated in Section 14.2.2 using the cavity model, a rectangular microstrip antenna can be represented as an array of two *radiating* narrow apertures (slots), each of width W and height h, separated by a distance L. Basically the transmission line model represents the microstrip antenna by two slots, separated by a low-impedance Z_c transmission line of length L.

A. Fringing Effects

Because the dimensions of the patch are finite along the length and width, the fields at the edges of the patch undergo fringing. This is illustrated along the length in Figures 14.1(a,b) for the two radiating slots of the microstrip antenna. The same applies along the width. The amount of fringing is a function of the dimensions of the patch and the height of the substrate. For the principal E-plane (xy-plane) fringing is a function of the ratio of the length of the patch L to the height h of the substrate (L/h) and the dielectric constant ϵ_r of the substrate. Since for microstrip antennas $L/h \gg 1$, fringing is reduced; however, it must be taken into account because it influences the resonant frequency of the antenna. The same applies for the width.

For a microstrip line shown in Figure 14.5(a), typical electric field lines are shown in Figure 14.5(b). This is a nonhomogeneous line of two dielectrics; typically the substrate and air. As can be seen, most of the electric field lines reside in the substrate and parts of some lines exist in air. As $W/h \gg 1$ and $\epsilon_r \gg 1$, the electric field lines concentrate mostly in the substrate. Fringing in this case makes the microstrip line look wider electrically compared to its physical dimensions. Since some of the waves travel in the substrate and some in air, an *effective dielectric constant* ϵ_{reff} is introduced to account for fringing and the wave propagation in the line.

To introduce the effective dielectric constant, let us assume that the center conductor of the microstrip line with its original dimensions and height above the ground plane is embedded into one dielectric, as shown in Figure 14.5(c). The effective dielectric constant is defined *as the dielectric constant of the uniform dielectric material so that the line of Figure 14.5(c) has identical electrical characteristics, particularly propagation constant, as the actual line of Figure 14.5(a).* For a line with air above the substrate, the effective dielectric constant has values in the range of $1 < \epsilon_{\text{reff}} < \epsilon_r$. For most applications where the dielectric constant of the substrate is much greater than unity ($\epsilon_r \gg 1$), the value of ϵ_{reff} will be closer to the value of the actual dielectric constant ϵ_r of the substrate. The effective dielectric constant is also a function of frequency. As the frequency of operation increases, most of the electric field lines concentrate in the substrate. Therefore the microstrip line behaves more like a homogeneous line of one dielectric (only the substrate), and the effective dielectric constant approaches the value of the dielectric constant of the substrate. Typical variations, as a function of frequency, of the effective dielectric constant for a microstrip line with three different substrates are shown in Figure 14.6.

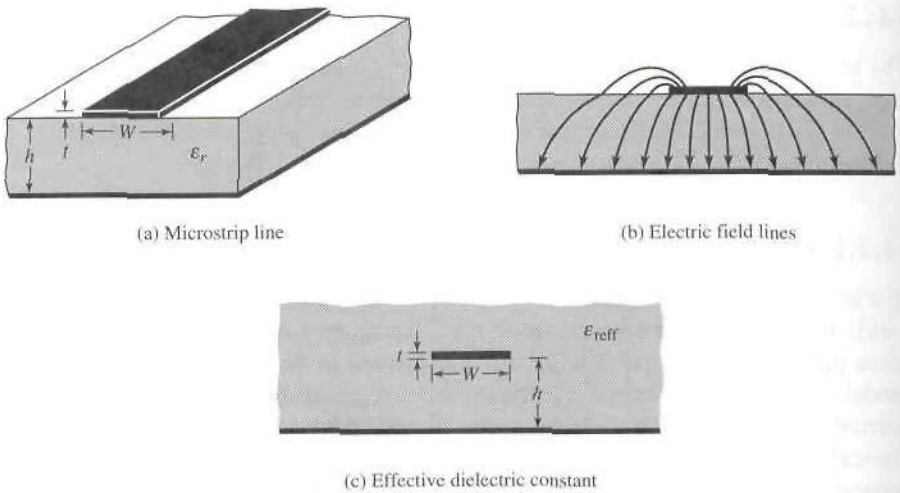

(a) Microstrip line

(b) Electric field lines

(c) Effective dielectric constant

Figure 14.5 Microstrip line and its electric field lines, and effective dielectric constant geometry.

For low frequencies the effective dielectric constant is essentially constant. At intermediate frequencies its values begin to monotonically increase and eventually approach the values of the dielectric constant of the substrate. The initial values (at low frequencies) of the effective dielectric constant are referred to as the *static values*, and they are given by [79]

$$\underline{W/h > 1}$$

$$\epsilon_{reff} = \frac{\epsilon_r + 1}{2} + \frac{\epsilon_r - 1}{2}\left[1 + 12\frac{h}{W}\right]^{-1/2} \tag{14-1}$$

B. Effective Length, Resonant Frequency, and Effective Width

Because of the fringing effects, electrically the patch of the microstrip antenna looks greater than its physical dimensions. For the principal *E*-plane (*xy*-plane), this is

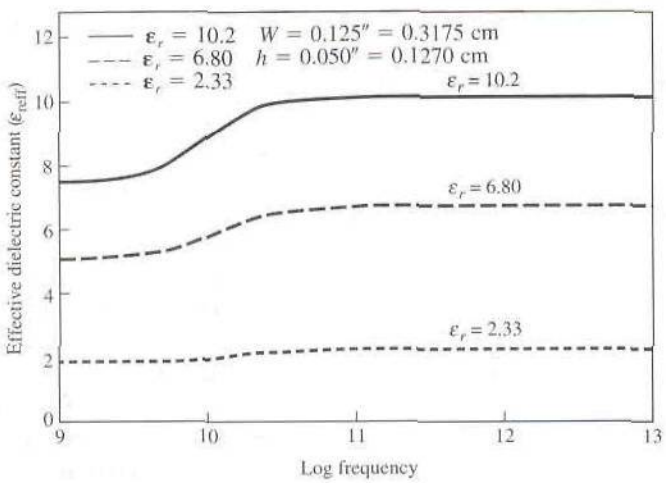

Figure 14.6 Effective dielectric constant versus frequency for typical substrates.

demonstrated in Figure 14.7 where the dimensions of the patch along its length have been extended on each end by a distance ΔL, which is a function of the effective dielectric constant ϵ_{reff} and the width-to-height ratio (W/h). A very popular and practical approximate relation for the normalized extension of the length is [80]

$$\frac{\Delta L}{h} = 0.412 \frac{(\epsilon_{reff} + 0.3)\left(\frac{W}{h} + 0.264\right)}{(\epsilon_{reff} - 0.258)\left(\frac{W}{h} + 0.8\right)} \tag{14-2}$$

Since the length of the patch has been extended by ΔL on each side, the effective length of the patch is now ($L = \lambda/2$ for dominant TM_{010} mode with no fringing)

$$L_{eff} = L + 2\Delta L \tag{14-3}$$

For the dominant TM_{010} mode, the resonant frequency of the microstrip antenna is a function of its length. Usually it is given by

$$(f_r)_{010} = \frac{1}{2L\sqrt{\epsilon_r}\sqrt{\mu_0\epsilon_0}} = \frac{v_0}{2L\sqrt{\epsilon_r}} \tag{14-4}$$

where v_0 is the speed of light in free space. Since (14-4) does not account for fringing, it must be modified to include edge effects and should be computed using

$$\begin{aligned}(f_{rc})_{010} &= \frac{1}{2L_{eff}\sqrt{\epsilon_{reff}}\sqrt{\mu_0\epsilon_0}} = \frac{1}{2(L + 2\Delta L)\sqrt{\epsilon_{reff}}\sqrt{\mu_0\epsilon_0}} \\ &= q\frac{1}{2L\sqrt{\epsilon_r}\sqrt{\mu_0\epsilon_0}} = q\frac{v_0}{2L\sqrt{\epsilon_r}}\end{aligned} \tag{14-5}$$

where

$$q = \frac{(f_{rc})_{010}}{(f_r)_{010}} \tag{14-5a}$$

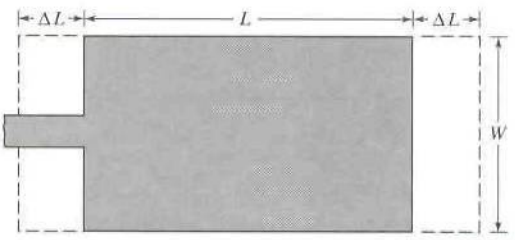

(a) Top view

(b) Side view

Figure 14.7 Physical and effective lengths of rectangular microstrip patch.

The q factor is referred to as the *fringe factor* (length reduction factor). As the substrate height increases, fringing also increases and leads to larger separations between the radiating edges and lower resonant frequencies.

C. Design

Based on the simplified formulation that has been described, a design procedure is outlined which leads to practical designs of rectangular microstrip antennas. The procedure assumes that the specified information includes the dielectric constant of the substrate (ϵ_r), the resonant frequency (f_r), and the height of the substrate h. The procedure is as follows:

Specify:

$$\epsilon_r, f_r \text{ (in Hz)}, \text{ and } h$$

Determine:

$$W, L$$

Design procedure:

1. For an efficient radiator, a practical width that leads to good radiation efficiencies is [15]

$$W = \frac{1}{2f_r\sqrt{\mu_0\epsilon_0}}\sqrt{\frac{2}{\epsilon_r + 1}} = \frac{v_0}{2f_r}\sqrt{\frac{2}{\epsilon_r + 1}} \tag{14-6}$$

   where v_0 is the free-space velocity of light.

2. Determine the effective dielectric constant of the microstrip antenna using (14-1).
3. Once W is found using (14-6), determine the extension of the length ΔL using (14-2).
4. The actual length of the patch can now be determined by solving (14-5) for L, or

$$L = \frac{1}{2f_r\sqrt{\epsilon_{reff}}\sqrt{\mu_0\epsilon_0}} - 2\Delta L \tag{14-7}$$

Example 14.1

Design a rectangular microstrip antenna using a substrate (RT/duroid 5880) with dielectric constant of 2.2, $h = 0.1588$ cm (0.0625 inches) so as to resonate at 10 GHz.

SOLUTION

Using (14-6), the width W of the patch is

$$W = \frac{30}{2(10)}\sqrt{\frac{2}{2.2 + 1}} = 1.186 \text{ cm } (0.467 \text{ in})$$

The effective dielectric constant of the patch is found using (14-1), or

$$\epsilon_{reff} = \frac{2.2 + 1}{2} + \frac{2.2 - 1}{2}\left(1 + 12\frac{0.1588}{1.186}\right)^{-1/2} = 1.972$$

The extended incremental length of the patch ΔL is, using (14-2)

$$\Delta L = 0.1588(0.412)\frac{(1.972 + 0.3)\left(\frac{1.186}{0.1588} + 0.264\right)}{(1.972 - 0.258)\left(\frac{1.186}{0.1588} + 0.8\right)}$$

$$= 0.081 \text{ cm } (0.032 \text{ in})$$

The actual length L of the patch is found using (14-3), or

$$L = \frac{\lambda}{2} - 2\Delta L = \frac{30}{2(10)\sqrt{1.972}} - 2(0.081) = 0.906 \text{ cm } (0.357 \text{ in})$$

Finally the effective length is

$$L_e = L + 2\Delta L = \frac{\lambda}{2} = 1.068 \text{ cm } (0.421 \text{ in})$$

D. Conductance

Each radiating slot is represented by a parallel equivalent admittance Y (with conductance G and susceptance B). This is shown in Figure 14.8. The slots are labeled as #1 and #2. The equivalent admittance of slot #1, based on an infinitely wide, uniform slot, is derived in Example 12.8 of Chapter 12, and it is given by [81]

$$Y_1 = G_1 + jB_1 \tag{14-8}$$

where for a slot of finite width W

$$G_1 = \frac{W}{120\lambda_0}\left[1 - \frac{1}{24}(k_0 h)^2\right] \qquad \frac{h}{\lambda_0} < \frac{1}{10} \tag{14-8a}$$

$$B_1 = \frac{W}{120\lambda_0}[1 - 0.636 \ln (k_0 h)] \qquad \frac{h}{\lambda_0} < \frac{1}{10} \tag{14-8b}$$

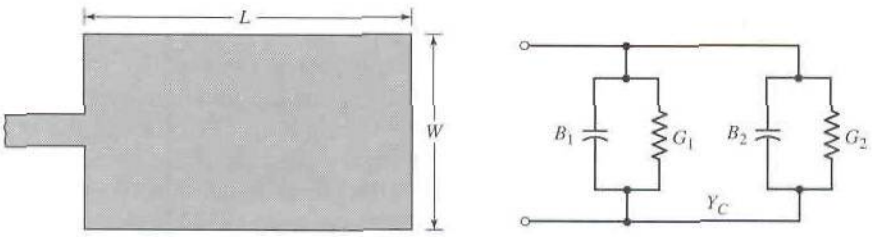

(a) Rectangular patch (b) Transmission model equivalent

Figure 14.8 Rectangular microstrip patch and its equivalent circuit transmission model.

Since slot #2 is identical to slot #1, its equivalent admittance is

$$Y_2 = Y_1, \qquad G_2 = G_1, \qquad B_2 = B_1 \tag{14-9}$$

The conductance of a single slot can also be obtained by using the field expression derived by the cavity model. In general, the conductance is defined as

$$G_1 = \frac{2P_{\text{rad}}}{|V_0|^2} \tag{14-10}$$

Using the electric field of (14-41), the radiated power is written as

$$P_{\text{rad}} = \frac{|V_0|^2}{2\pi\eta_0} \int_0^{\pi} \left[\frac{\sin\left(\frac{k_0 W}{2} \cos\theta\right)}{\cos\theta} \right]^2 \sin^3\theta \, d\theta \tag{14-11}$$

Therefore the conductance of (14-10) can be expressed as

$$G_1 = \frac{I_1}{120\pi^2} \tag{14-12}$$

where

$$I_1 = \int_0^{\pi} \left[\frac{\sin\left(\frac{k_0 W}{2} \cos\theta\right)}{\cos\theta} \right]^2 \sin^3\theta \, d\theta$$

$$= -2 + \cos(X) + XS_i(X) + \frac{\sin(X)}{X} \tag{14-12a}$$

$$X = k_0 W \tag{14-12b}$$

Asymptotic values of (14-12) and (14-12a) are

$$G_1 = \begin{cases} \dfrac{1}{90}\left(\dfrac{W}{\lambda_0}\right)^2 & W \ll \lambda_0 \\ \dfrac{1}{120}\left(\dfrac{W}{\lambda_0}\right) & W \gg \lambda_0 \end{cases} \tag{14-13}$$

The values of (14-13) for $W \gg \lambda_0$ are identical to those given by (14-8a) for $h \ll \lambda_0$. A plot of G as a function of W/λ_0 is shown in Figure 14.9.

E. Resonant Input Resistance

The total admittance at slot #1 (input admittance) is obtained by transferring the admittance of slot #2 from the output terminals to input terminals using the admittance transformation equation of transmission lines [16], [70], [79]. Ideally the two slots should be separated by $\lambda/2$ where λ is the wavelength in the dielectic (substrate). However, because of fringing the length of the patch is electrically longer than the actual length. Therefore the actual separation of the two slots is slightly less than $\lambda/2$. If the reduction of the length is properly chosen using (14-2) (typically $0.48\lambda < L < 0.49\lambda$), the transformed admittance of slot #2 becomes

$$\tilde{Y}_2 = \tilde{G}_2 + j\tilde{B}_2 = G_1 - jB_1 \tag{14-14}$$

or

$$\tilde{G}_2 = G_1 \tag{14-14a}$$

$$\tilde{B}_2 = -B_1 \tag{14-14b}$$

Therefore the total resonant input admittance is real and is given by

$$Y_{in} = Y_1 + \tilde{Y}_2 = 2G_1 \tag{14-15}$$

Since the total input admittance is real, the resonant input impedance is also real, or

$$Z_{in} = \frac{1}{Y_{in}} = R_{in} = \frac{1}{2G_1}. \tag{14-16}$$

The resonant input resistance, as given by (14-16), does not take into account mutual effects between the slots. This can be accomplished by modifying (14-16) to [8]

$$R_{in} = \frac{1}{2(G_1 \pm G_{12})} \tag{14-17}$$

where the plus (+) sign is used for modes with odd (antisymmetric) resonant voltage distribution beneath the patch and between the slots while the minus (−) sign is used for modes with even (symmetric) resonant voltage distribution. The mutual conductance is defined, in terms of the far-zone fields, as

$$G_{12} = \frac{1}{|V_0|^2} \text{Re} \iint_S \mathbf{E}_1 \times \mathbf{H}_2^* \cdot d\mathbf{s} \tag{14-18}$$

where $\mathbf{E}_1$ is the electric field radiated by slot #1, $\mathbf{H}_2$ is the magnetic field radiated by slot #2, V_0 is the voltage across the slot, and the integration is performed over a sphere of large radius. It can be shown that G_{12} can be calculated using [8], [34]

$$G_{12} = \frac{1}{120\pi^2} \int_0^{\pi} \left[\frac{\sin\left(\frac{k_0 W}{2} \cos\theta\right)}{\cos\theta} \right]^2 J_0(k_0 L \sin\theta) \sin^3\theta \, d\theta \tag{14-18a}$$

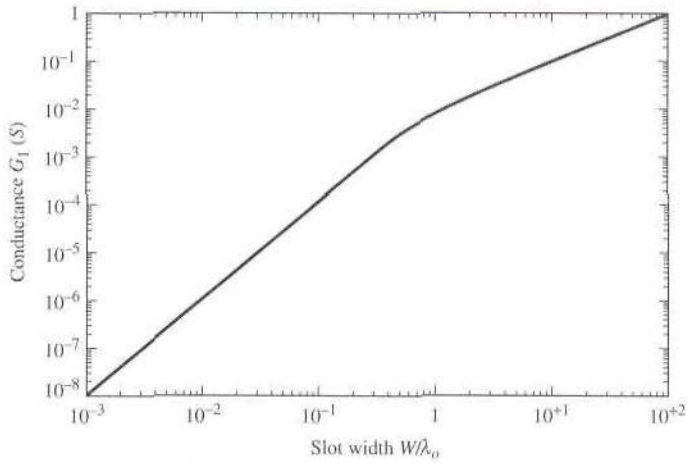

Figure 14.9 Slot conductance as a function of slot width.

where J_0 is the Bessel function of the first kind of order zero. For typical microstrip antennas, the mutual conductance obtained using (14-18a) is small compared to the self conductance G_1 of (14-8a) or (14-12).

As shown by (14-8a) and (14-17), the input resistance is not strongly dependent upon the substrate height h. In fact for very small values of h, such that $k_0 h \ll 1$, the input resistance is not dependent on h. Modal-expansion analysis also reveals that the input resistance is not strongly influenced by the substrate height h. It is apparent from (14-8a) and (14-17) that the resonant input resistance can be decreased by increasing the width W of the patch. This is acceptable as long as the ratio of W/L does not exceed 2 because the aperture efficiency of a single patch begins to drop, as W/L increases beyond 2.

The resonant input resistance, as calculated by (14-17), is referenced at slot #1. However, it has been shown that the resonant input resistance can be changed by using an inset feed, recessed a distance y_0 from slot #1, as shown in Figure 14.10(a). This technique can be used effectively to match the patch antenna using a microstrip-line feed whose characteristic impedance is given by [79]

$$Z_c = \begin{cases} \dfrac{60}{\sqrt{\epsilon_{\text{reff}}}} \ln\left[\dfrac{8h}{W_0} + \dfrac{W_0}{4h}\right], & \dfrac{W_0}{h} \le 1 \quad (14\text{-}19a) \\ \dfrac{120\pi}{\sqrt{\epsilon_{\text{reff}}}\left[\dfrac{W_0}{h} + 1.393 + 0.667 \ln\left(\dfrac{W_0}{h} + 1.444\right)\right]}, & \dfrac{W_0}{h} > 1 \quad (14\text{-}19b) \end{cases}$$

where W_0 is the width of the microstrip line, as shown in Figure 14.10. Using modal-expansion analysis, the input resistance for the inset-feed is given approximately by [8], [16]

$$R_{\text{in}}(y = y_0) = \frac{1}{2(G_1 \pm G_{12})}\left[\cos^2\left(\frac{\pi}{L}y_0\right) + \frac{G_1^2 + B_1^2}{Y_c^2}\sin^2\left(\frac{\pi}{L}y_0\right) - \frac{B_1}{Y_c}\sin\left(\frac{2\pi}{L}y_0\right)\right] \quad (14\text{-}20)$$

where $Y_c = 1/Z_c$. Since for most typical microstrips $G_1/Y_c \ll 1$ and $B_1/Y_c \ll 1$, (14-20) reduces to

$$R_{\text{in}}(y = y_0) = \frac{1}{2(G_1 \pm G_{12})}\cos^2\left(\frac{\pi}{L}y_0\right) = R_{\text{in}}(y = 0)\cos^2\left(\frac{\pi}{L}y_0\right) \quad (14\text{-}20a)$$

A plot of the normalized value of (14-20a) is shown in Figure 14.10(b).

The values obtained using (14-20) agree fairly well with experimental data. However, the inset feed introduces a physical notch, which in turn introduces a junction capacitance. The physical notch and its corresponding junction capacitance influence slightly the resonance frequency, which typically may vary by about 1%. It is apparent from (14-20a) and Figure 14.10(b) that the maximum value occurs at the edge of the slot ($y_0 = 0$) where the voltage is maximum and the current is minimum; typical values are in the 150–300 ohms. The minimum value (zero) occurs at the

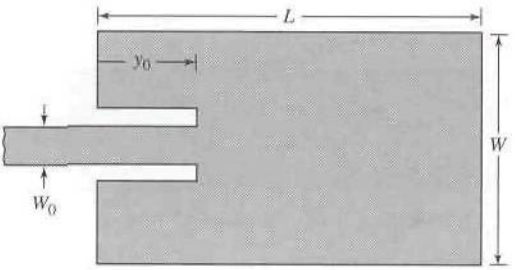

(a) Recessed microstrip-line feed

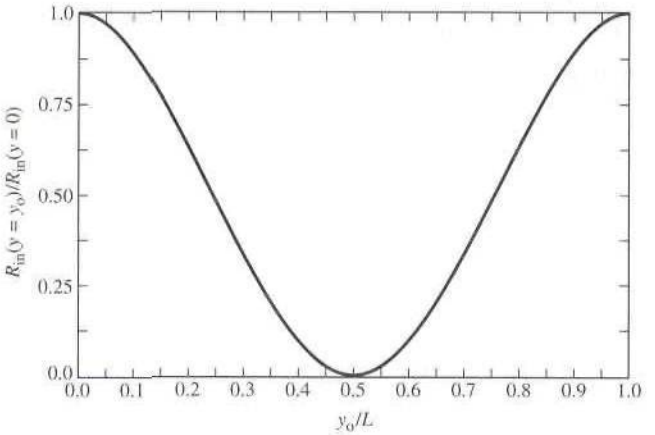

(b) Normalized input resistance

Figure 14.10 Recessed microstrip-line feed and variation of normalized input resistance.

center of the patch ($y_0 = L/2$) where the voltage is zero and the current is maximum. As the inset feed-point moves from the edge toward the center of the patch the resonant input impedance decreases monotonically and reaches zero at the center. When the value of the inset feed-point approaches the center of the patch ($y_0 = L/2$), the $\cos^2(\pi y_0/L)$ function varies very rapidly; therefore the input resistance also changes rapidly with the position of the feed point. To maintain very accurate values, a close tolerance must be preserved.

Example 14.2

A microstrip antenna with overall dimensions of $L = 0.906$ cm (0.357 inches) and $W = 1.186$ cm (0.467 inches), substrate with height $h = 0.1588$ cm (0.0625 inches) and dielectric constant of $\epsilon_r = 2.2$, is operating at 10 GHz. Find:

a. The input impedance.

b. The position of the inset feed-point where the input impedance is 50 ohms.

SOLUTION

$$\lambda_0 = \frac{30}{10} = 3 \text{ cm}$$

Using (14-12) and (14-12a)

$$G_1 = 0.00157 \text{ siemens}$$

which compares with $G_1 = 0.00328$ using (14-8a). Using (14-18a)

$$G_{12} = 6.1683 \times 10^{-4}$$

Using (14-17) with the (+) sign because of the odd field distribution between the radiating slots for the dominant TM_{010} mode

$$R_{in} = 228.3508 \text{ ohms.}$$

Since the input impedance at the leading radiating edge of the patch is 228.3508 ohms while the desired impedance is 50 ohms, the inset feet-point distance y_0 is obtained using (14-20a). Thus

$$50 = 228.3508 \cos^2\left(\frac{\pi}{L} y_0\right)$$

or

$$y_0 = 0.3126 \text{ cm } (0.123 \text{ inches})$$

14.2.2 Cavity Model

Microstrip antennas resemble dielectric loaded cavities, and they exhibit higher order resonances. The normalized fields within the dielectric substrate (between the patch and the ground plane) can be found more accurately by treating that region as a cavity bounded by electric conductors (above and below it) and by magnetic walls (to simulate an open circuit) along the perimeter of the patch. This is an approximate model, which in principle leads to a reactive input impedance (of zero or infinite value of resonance), and it does not radiate any power. However, assuming that the actual fields are approximate to those generated by such a model, the computed pattern, input admittance, and resonant frequencies compare well with measurements [12], [16], [18]. This is an accepted approach, and it is similar to the perturbation methods which have been very successful in the analysis of waveguides, cavities, and radiators [81].

To shed some insight into the cavity model, let us attempt to present a physical interpretation into the formation of the fields within the cavity and radiation through its side walls. When the microstrip patch is energized, a charge distribution is established on the upper and lower surfaces of the patch, as well as on the surface of the ground plane, as shown in Figure 14.11. The charge distribution is controlled by two mechanisms; an *attractive* and a *repulsive* mechanism [34]. The *attractive* mechanism is between the corresponding opposite charges on the bottom side of the patch and the ground plane, which tends to maintain the charge concentration on the bottom of the patch. The *repulsive* mechanism is between like charges on the bottom surface of the patch, which tends to push some charges from the bottom of the patch, around its

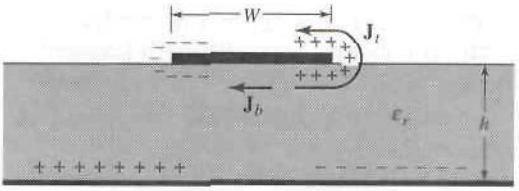

Figure 14.11 Charge distribution and current density creation on microstrip patch.

edges, to its top surface. The movement of these charges creates corresponding current densities $\mathbf{J}_b$ and $\mathbf{J}_t$, at the bottom and top surfaces of the patch, respectively, as shown in Figure 14.11. Since for most practical microstrips the height-to-width ratio is very small, the attractive mechanism dominates and most of the charge concentration and current flow remain underneath the patch. A small amount of current flows around the edges of the patch to its top surface. However, this current flow decreases as the height-to-width ratio decreases. In the limit, the current flow to the top would be zero, which ideally would not create any tangential magnetic field components to the edges of the patch. This would allow the four side walls to be modelled by perfect magnetic conducting surfaces which ideally would not disturb the magnetic field and, in turn, the electric field distributions beneath the patch. Since in practice there is a finite height-to-width ratio, although small, the tangential magnetic fields at the edges would not be exactly zero. However, since they will be small, a good approximation to the cavity model is to treat the side walls as perfectly magnetic conducting. This model produces good normalized electric and magnetic field distributions (modes) beneath the patch.

If the microstrip antenna were treated only as a cavity, it would not be sufficient to find the absolute amplitudes of the electric and magnetic fields. In fact by treating the walls of the cavity, as well as the material within it as lossless, the cavity would not radiate and its input impedance would be purely reactive. Also the function representing the impedance would only have real poles. To account for radiation, a loss mechanism has to be introduced. In Figure 2.21 of Chapter 2, this was taken into account by the radiation resistance R_r and loss resistance R_L. These two resistances allow the input impedance to be complex and for its function to have complex poles; the imaginary poles representing, through R_r and R_L, the radiation and conduction-dielectric losses. To make the microstrip lossy using the cavity model, which would then represent an antenna, the loss is taken into account by introducing an effective loss tangent δ_{eff}. The effective loss tangent is chosen appropriately to represent the loss mechanism of the cavity, which now behaves as an antenna and is taken as the reciprocal of the antenna quality factor Q ($\delta_{\text{eff}} = 1/Q$).

Because the thickness of the microstrip is usually very small, the waves generated within the dielectric substrate (between the patch and the ground plane) undergo considerable reflections when they arrive at the edge of the patch. Therefore only a small fraction of the incident energy is radiated; thus the antenna is considered to be very inefficient. The fields beneath the patch form standing waves that can be represented by cosinusoidal wave functions. Since the height of the substrate is very small ($h \ll \lambda$ where λ is the wavelength within the dielectric), the field variations along the height will be considered constant. In addition, because of the very small substrate height, the fringing of the fields along the edges of the patch are also very small whereby the electric field is nearly normal to the surface of the patch. Therefore only TM^x field configurations will be considered within the cavity. While the top and

bottom walls of the cavity are perfectly electric conducting, the four side walls will be modeled as perfectly conducting magnetic walls (tangential magnetic fields vanish along those four walls).

A. Field Configurations (modes)—TM^x

The field configurations within the cavity can be found using the vector potential approach described in detail in Chapter 8 of [79]. Referring to Figure 14.12, the volume beneath the patch can be treated as a rectangular cavity loaded with a dielectric material with dielectric constant ϵ_r. The dielectric material of the substrate is assumed to be truncated and not extended beyond the edges of the patch. The vector potential A_x must satisfy the homogeneous wave equation of

$$\nabla^2 A_x + k^2 A_x = 0 \tag{14-21}$$

whose solution is written in general, using the separation of variables, as [79]

$$\begin{aligned} A_x = {} & [A_1 \cos(k_x x) + B_1 \sin(k_x x)][A_2 \cos(k_y y) + B_2 \sin(k_y y)] \\ & \cdot [A_3 \cos(k_z z) + B_3 \sin(k_z z)] \end{aligned} \tag{14-22}$$

where k_x, k_y and k_z are the wavenumbers along the x, y and z directions, respectively. These will be determined subject to the boundary conditions. The electric and magnetic fields within the cavity are related to the vector potential A_x by [79]

$$\begin{aligned} E_x &= -j\frac{1}{\omega\mu\epsilon}\left(\frac{\partial^2}{\partial x^2} + k^2\right)A_x & H_x &= 0 \\ E_y &= -j\frac{1}{\omega\mu\epsilon}\frac{\partial^2 A_x}{\partial x \partial y} & H_y &= \frac{1}{\mu}\frac{\partial A_x}{\partial z} \\ E_z &= -j\frac{1}{\omega\mu\epsilon}\frac{\partial^2 A_x}{\partial x \partial z} & H_z &= -\frac{1}{\mu}\frac{\partial A_x}{\partial y} \end{aligned} \tag{14-23}$$

subject to the boundary conditions of

$$\begin{aligned} & E_y(x' = 0, 0 \le y' \le L, 0 \le z' \le W) \\ & \quad = E_y(x' = h, 0 \le y' \le L, 0 \le z' \le W) = 0 \\ & H_y(0 \le x' \le h, 0 \le y' \le L, z' = 0) \\ & \quad = H_y(0 \le x' \le h, 0 \le y' \le L, z' = W) = 0 \\ & H_z(0 \le x' \le h, y' = 0, 0 \le z' \le W) \\ & \quad = H_z(0 \le x' \le h, y' = L, 0 \le z' \le W) = 0 \end{aligned} \tag{14-24}$$

The primed coordinates x', y', z' are used to represent the fields within the cavity.

Applying the boundary conditions $E_y(x' = 0, 0 \le y' \le L, 0 \le z' \le W) = 0$ and $E_y(x' = h, 0 \le y' \le L, 0 \le z' \le W) = 0$, it can be shown that $B_1 = 0$ and

$$k_x = \frac{m\pi}{h}, \qquad m = 0, 1, 2, \ldots . \tag{14-25}$$

Similarly, applying the boundary conditions $H_y(0 \le x' \le h, 0 \le y' \le L, z' = 0) = 0$ and $H_y(0 \le x' \le h, 0 \le y' \le L, z' = W) = 0$, it can be shown that $B_3 = 0$ and

$$k_z = \frac{p\pi}{W}, \qquad p = 0, 1, 2, \ldots . \tag{14-26}$$

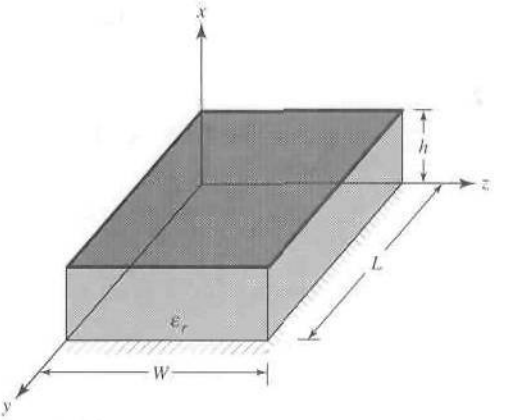

Figure 14.12 Rectangular microstrip patch geometry.

Finally, applying the boundary conditions $H_z(0 \le x' \le h,\ y' = 0,\ 0 \le z' \le W) = 0$ and $H_z(0 \le x' \le h,\ y' = L,\ 0 \le z' \le W) = 0$, it can be shown that $B_2 = 0$ and

$$k_y = \frac{n\pi}{L}, \qquad n = 0, 1, 2, \ldots . \tag{14-27}$$

Thus the final form for the vector potential A_x within the cavity is

$$A_x = A_{mnp} \cos(k_x x') \cos(k_y y') \cos(k_z z') \tag{14-28}$$

where A_{mnp} represents the amplitude coefficients of each mnp mode. The wavenumbers k_x, k_y, k_z are equal to

$$\left.\begin{aligned} k_x &= \left(\frac{m\pi}{h}\right), \quad m = 0, 1, 2, \ldots \\ k_y &= \left(\frac{n\pi}{L}\right), \quad n = 0, 1, 2, \ldots \\ k_z &= \left(\frac{p\pi}{W}\right), \quad p = 0, 1, 2, \ldots \end{aligned}\right\} m = n = p \neq 0 \tag{14-29}$$

where m, n, p represent, respectively, the number of half-cycle field variations along the x, y, z directions.

Since the wavenumbers k_x, k_y, and k_z are subject to the constraint equation

$$k_x^2 + k_y^2 + k_z^2 = \left(\frac{m\pi}{h}\right)^2 + \left(\frac{n\pi}{L}\right)^2 + \left(\frac{p\pi}{W}\right)^2 = k_r^2 = \omega_r^2 \mu\epsilon \tag{14-30}$$

the resonant frequencies for the cavity are given by

$$(f_r)_{mnp} = \frac{1}{2\pi\sqrt{\mu\epsilon}} \sqrt{\left(\frac{m\pi}{h}\right)^2 + \left(\frac{n\pi}{L}\right)^2 + \left(\frac{p\pi}{W}\right)^2} \tag{14-31}$$

Substituting (14-28) into (14-23), the electric and magnetic fields within the cavity are written as

$$
\begin{aligned}
E_x &= -j\frac{(k^2 - k_x^2)}{\omega\mu\epsilon} A_{mnp} \cos(k_x x') \cos(k_y y') \cos(k_z z') \\
E_y &= -j\frac{k_x k_y}{\omega\mu\epsilon} A_{mnp} \sin(k_x x') \sin(k_y y') \cos(k_z z') \\
E_z &= -j\frac{k_x k_z}{\omega\mu\epsilon} A_{mnp} \sin(k_x x') \cos(k_y y') \sin(k_z z') \\
H_x &= 0 \\
H_y &= -\frac{k_z}{\mu} A_{mnp} \cos(k_x x') \cos(k_y y') \sin(k_z z') \\
H_z &= \frac{k_y}{\mu} A_{mnp} \cos(k_x x') \sin(k_y y') \cos(k_z z')
\end{aligned}
\tag{14-32}
$$

To determine the dominant mode with the lowest resonance, we need to examine the resonant frequencies. The mode with the lowest order resonant frequency is referred to as the *dominant* mode. Placing the resonant frequencies in ascending order determines the order of the modes of operation. For all microstrip antennas $h \ll L$ and $h \ll W$. If $L > W > h$, the mode with the lowest frequency (dominant mode) is the TM^x_{010} whose resonant frequency is given by

$$
(f_r)_{010} = \frac{1}{2L\sqrt{\mu\epsilon}} = \frac{v_0}{2L\sqrt{\epsilon_r}} \tag{14-33}
$$

where v_0 is the speed of light in free space. If in addition $L > W > L/2 > h$, the next higher order (second) mode is the TM^x_{001} whose resonant frequency is given by

$$
(f_r)_{001} = \frac{1}{2W\sqrt{\mu\epsilon}} = \frac{v_0}{2W\sqrt{\epsilon_r}} \tag{14-34}
$$

If, however, $L > L/2 > W > h$, the second order mode is the TM^x_{020}, instead of the TM^x_{001}, whose resonant frequency is given by

$$
(f_r)_{020} = \frac{1}{L\sqrt{\mu\epsilon}} = \frac{v_0}{L\sqrt{\epsilon_r}} \tag{14-35}
$$

If $W > L > h$, the dominant mode is the TM^x_{001} whose resonant frequency is given by (14-34) while if $W > W/2 > L > h$ the second order mode is the TM^x_{002}. Based upon (14-32), the distribution of the tangential electric field along the side walls of the cavity for the TM^x_{010}, TM^x_{001}, TM^x_{020} and TM^x_{002} is as shown, respectively, in Figure 14.13.

In all of the preceding discussion, it was assumed that there is no fringing of the fields along the edges of the cavity. This is not totally valid, but it is a good assumption. However, fringing effects and their influence were discussed previously, and they should be taken into account in determining the resonant frequency. This was done in (14-5) for the dominant TM^x_{010} mode.

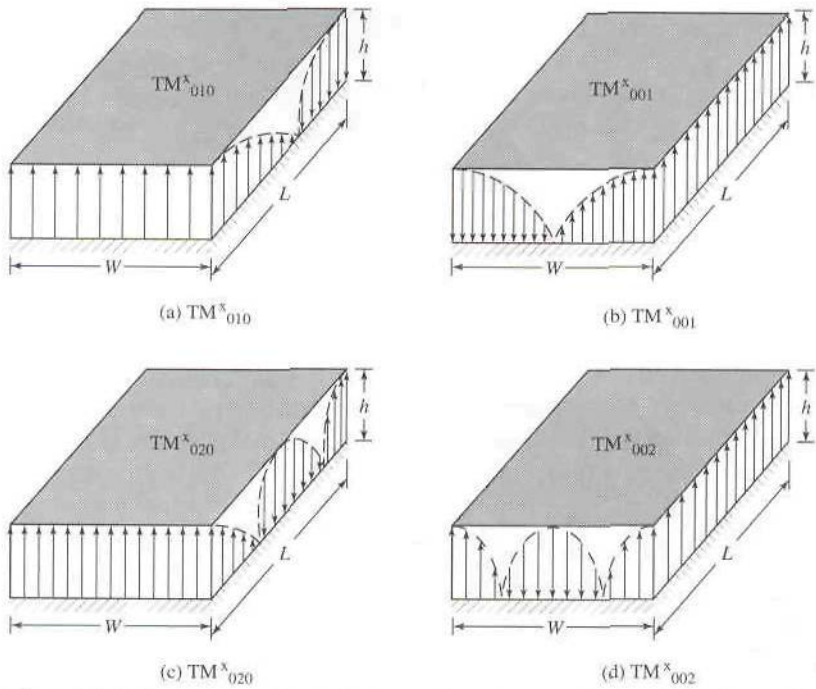

Figure 14.13 Field configurations (modes) for rectangular microstrip patch.

B. Equivalent Current Densities

It has been shown using the cavity model that the microstrip antenna can be modeled reasonably well by a dielectric-loaded cavity with two perfectly conducting electric walls (top and bottom), and four perfectly conducting magnetic walls (sidewalls). It is assumed that the material of the substrate is truncated and does not extend beyond the edges of the patch. The four sidewalls represent four narrow apertures (slots) through which radiation takes place. Using the Field Equivalence Principle (Huygens' Principle) of Section 12.2 of Chapter 12, the microstrip patch is represented by an equivalent electric current density $\mathbf{J}_t$ at the top surface of the patch to account for the presence of the patch (there is also a current density $\mathbf{J}_b$ at the bottom of the patch which is not needed for this model). The four side slots are represented by the equivalent electric current density $\mathbf{J}_s$ and equivalent magnetic current density $\mathbf{M}_s$, as shown in Figure 14.14(a), each represented by

$$\mathbf{J}_s = \hat{\mathbf{n}} \times \mathbf{H}_a \tag{14-36}$$

and

$$\mathbf{M}_s = -\hat{\mathbf{n}} \times \mathbf{E}_a \tag{14-37}$$

where $\mathbf{E}_a$ and $\mathbf{H}_a$ represent, respectively, the electric and magnetic fields at the slots.

Because it was shown that for microstrip antennas with very small height-to-width ratio the current density $\mathbf{J}_t$ at the top of the patch is much smaller than the current density $\mathbf{J}_b$ at the bottom of the patch, it will be assumed it is negligible here and it will be set to zero. Also it was argued that the tangential magnetic fields along the edges of the patch are very small, ideally zero. Therefore the corresponding equivalent electric current density $\mathbf{J}_s$ will be very small (ideally zero), and it will be

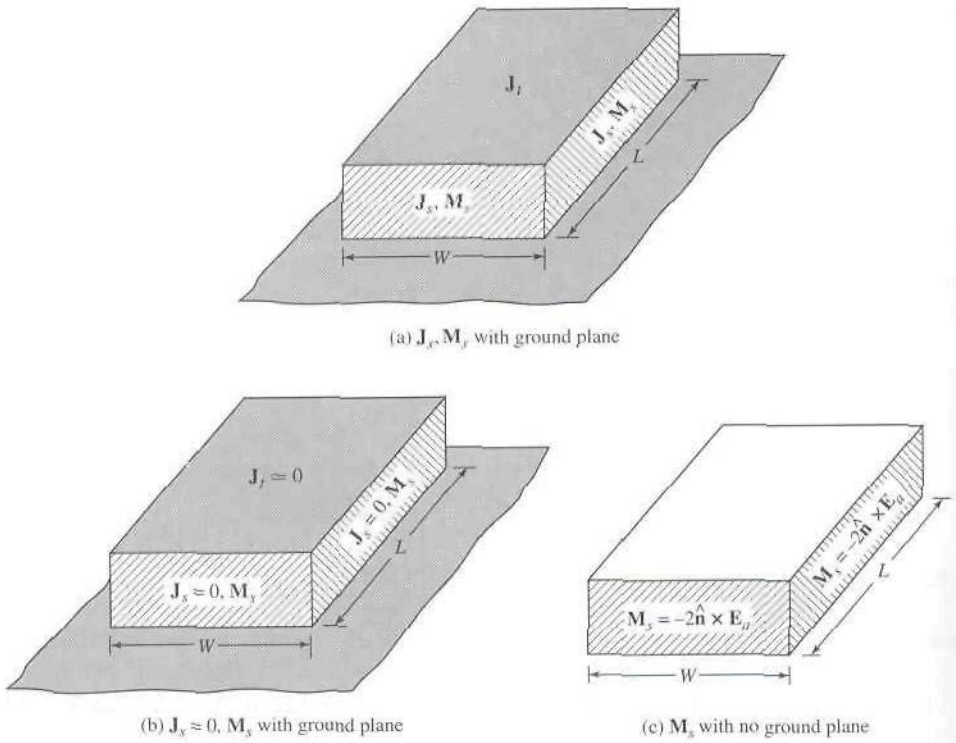

(a) $\mathbf{J}_s, \mathbf{M}_s$ with ground plane

(b) $\mathbf{J}_s \simeq 0$, $\mathbf{M}_s$ with ground plane

(c) $\mathbf{M}_s$ with no ground plane

Figure 14.14 Equivalent current densities on four sides of rectangular microstrip patch.

set to zero here. Thus the only nonzero current density is the equivalent magnetic current density $\mathbf{M}_s$ of (14-37) along the side periphery of the cavity radiating in the presence of the ground plane, as shown in Figure 14.14(b). The presence of the ground plane can be taken into account by image theory which will double the equivalent magnetic current density of (14-37). Therefore the final equivalent is a magnetic current density of twice (14-37) or

$$\mathbf{M}_s = -2\hat{\mathbf{n}} \times \mathbf{E}_a \tag{14-38}$$

around the side periphery of the patch radiating into free space, as shown in Figure 14.14(c).

It was shown, using the transmission-line model, that the microstrip antenna can be represented by two radiating slots along the length of the patch (each of width W and height h). Similarly it will be shown here also that while there are a total of four slots representing the microstrip antenna, only two (the radiating slots) account for most of the radiation; the fields radiated by the other two, which are separated by the width W of the patch, cancel along the principal planes. Therefore the same two slots, separated by the length of the patch, are referred to here also as *radiating* slots. The slots are separated by a very low impedance parallel-plate transmission line of length L, which acts as a transformer. The length of the transmission line is approximately $\lambda/2$, where λ is the guide wavelength in the substrate, in order for the fields at the aperture of the two slots to have opposite polarization. This is illustrated in Figures 14.1(a) and 14.13(a). The two slots form a two-element array with a spacing of $\lambda/2$ between the elements. It will be shown here that in a direction perpendicular to the

ground plane the components of the field add in phase and give a maximum radiation normal to the patch; thus broadside antenna.

Assuming that the dominant mode within the cavity is the TM^x_{010} mode, the electric and magnetic field components reduce from (14-32) to

$$E_x = E_0 \cos\left(\frac{\pi}{L}y'\right)$$
$$H_z = H_0 \sin\left(\frac{\pi}{L}y'\right) \tag{14-39}$$
$$E_y = E_z = H_x = H_y = 0$$

where $E_0 = -j\omega A_{010}$ and $H_0 = (\pi/\mu L) A_{010}$. The electric field structure within the substrate and between the radiating element and the ground plane is sketched in Figures 14.1(a,b) and 14.13(a). It undergoes a phase reversal along the length but it is uniform along its width. The phase reversal along the length is necessary for the antenna to have broadside radiation characteristics.

Using the equivalence principle of Section 12.3, each slot radiates the same fields as a magnetic dipole with current density $\mathbf{M}_s$ equal to (14-38). By referring to Figures 14.15 the equivalent magnetic current densities along the two slots, each of width W and height h, are both of the same magnitude and of the same phase. Therefore these two slots form a two-element array with the sources (current densities) of the same magnitude and phase, and separated by L. Thus these two sources will add in a direction normal to the patch and ground plane forming a broadside pattern. This is illustrated in Figures 14.16(a) where the normalized radiation pattern of each slot in the principal E-plane is sketched individually along with the total pattern of the two. In the H-plane, the normalized pattern of each slot and of the two together is the same, as shown in Figure 14.16(b).

The equivalent current densities for the other two slots, each of length L and height h, are shown in Figure 14.17. Since the current densities on each wall are of the same magnitude but of opposite direction, the fields radiated by these two slots cancel each other in the principal H-plane. Also since corresponding slots on opposite walls are 180° out of phase, the corresponding radiations cancel each other in the principal E-plane. This will be shown analytically. The radiation from these two side walls in nonprincipal planes is small compared to the other two side walls. Therefore these two slots are usually referred to as *nonradiating* slots.

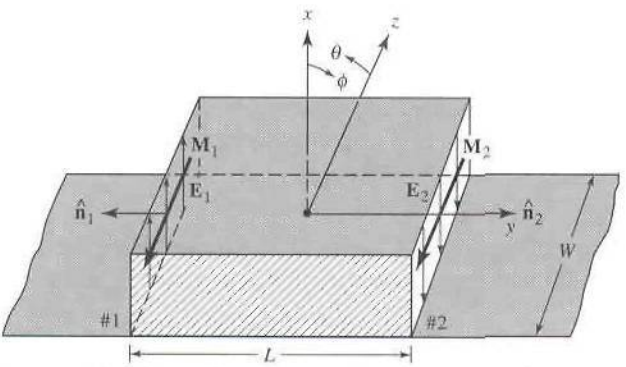

Figure 14.15 Rectangular microstrip patch radiating slots and equivalent magnetic current densities.

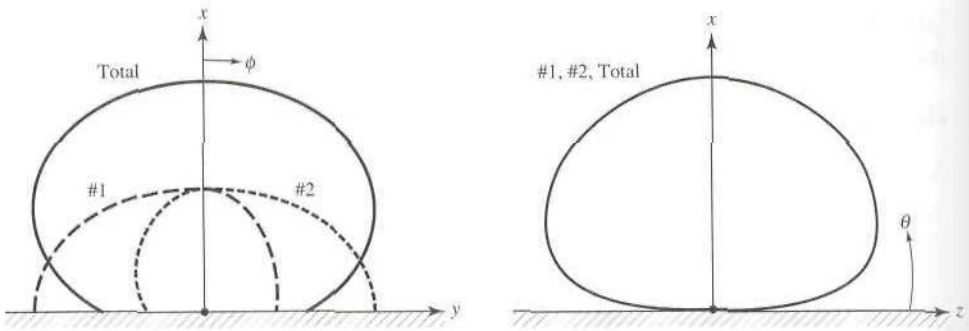

(a) E-plane (b) H-plane

Figure 14.16 Typical E- and H-plane patterns of each microstrip patch slot, and of the two together.

C. Fields Radiated—TM^x_{010} *Mode*

To find the fields radiated by each slot, we follow a procedure similar to that used to analyze the aperture in Section 12.5.1. The total field is the sum of the two-element array with each element representing one of the slots. Since the slots are identical, this is accomplished by using an array factor for the two slots.

Radiating Slots Following a procedure similar to that used to analyze the aperture in Section 12.5.1, the far-zone electric fields radiated by each slot, using the equivalent current densities of (14-38), are written as

$$E_r \simeq E_\theta \simeq 0 \tag{14-40a}$$

$$E_\phi = +j\frac{k_0 hW\,E_0 e^{-jk_0 r}}{2\pi r}\left\{\sin\theta\frac{\sin(X)}{X}\frac{\sin(Z)}{Z}\right\} \tag{14-40b}$$

where

$$X = \frac{k_0 h}{2}\sin\theta\cos\phi \tag{14-40c}$$

$$Z = \frac{k_0 W}{2}\cos\theta \tag{14-40d}$$

For very small heights ($k_0 h \ll 1$), (14-40b) reduces to

$$E_\phi \simeq +j\frac{V_0 e^{-jk_0 r}}{\pi r}\left\{\sin\theta\frac{\sin\left(\dfrac{k_0 W}{2}\cos\theta\right)}{\cos\theta}\right\} \tag{14-41}$$

where $V_0 = hE_0$.

According to the theory of Chapter 6, the array factor for the two elements, of the same magnitude and phase, separated by a distance L_e along the y direction is

$$(AF)_y = 2\cos\left(\frac{k_0 L_e}{2}\sin\theta\sin\phi\right) \tag{14-42}$$

where L_e is the effective length of (14-3). Thus, the total electric field for the two slots (also for the microstrip antenna) is

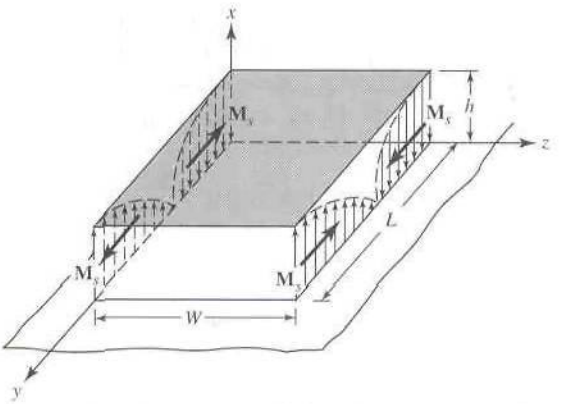

Figure 14.17 Current densities on nonradiating slots of rectangular microstrip patch.

$$E_\phi^t = +j\frac{k_0 hW E_0 e^{-jk_0 r}}{\pi r}\left\{\sin\theta\frac{\sin(X)}{X}\frac{\sin(Z)}{Z}\right\} \times \cos\left(\frac{k_0 L_e}{2}\sin\theta\sin\phi\right) \tag{14-43}$$

where

$$X = \frac{k_0 h}{2}\sin\theta\cos\phi \tag{14-43a}$$

$$Z = \frac{k_0 W}{2}\cos\theta \tag{14-43b}$$

For small values of h ($k_0 h \ll 1$), (14-43) reduces to

$$E_\phi^t \simeq +j\frac{2V_0 e^{-jk_0 r}}{\pi r}\left\{\sin\theta\frac{\sin\left(\frac{k_0 W}{2}\cos\theta\right)}{\cos\theta}\right\}\cos\left(\frac{k_0 L_e}{2}\sin\theta\sin\phi\right) \tag{14-44}$$

where $V_0 = hE_0$ is the voltage across the slot.

***E-Plane* ($\theta = 90°$, $0° \le \phi \le 90°$ and $270° \le \phi \le 360°$)**

For the microstrip antenna, the x-y plane ($\theta = 90°$, $0° \le \phi \le 90°$ and $270° \le \phi \le 360°$) is the principal E-plane. For this plane, the expressions for the radiated fields of (14-43)–(14-43b) reduce to

$$E_\phi^t = +j\frac{k_0 WV_0 e^{-jk_0 r}}{\pi r}\left\{\frac{\sin\left(\frac{k_0 h}{2}\cos\phi\right)}{\frac{k_0 h}{2}\cos\phi}\right\}\cos\left(\frac{k_0 L_e}{2}\sin\phi\right) \tag{14-45}$$

***H-Plane* ($\phi = 0°$, $0° \le \theta \le 180°$)**

The principal H-plane of the microstrip antenna is the x-z plane ($\phi = 0°$, $0° \le \theta \le 180°$), and the expressions for the fields radiated of (14-43)–(14-43b) reduce to

$$E_\phi^t \simeq +j\frac{k_0\, WV_0 e^{-jk_0 r}}{\pi r}\left\{\sin\theta\,\frac{\sin\left(\frac{k_0 h}{2}\sin\theta\right)}{\frac{k_0 h}{2}\sin\theta}\,\frac{\sin\left(\frac{k_0 W}{2}\cos\theta\right)}{\frac{k_0 W}{2}\cos\theta}\right\} \tag{14-46}$$

To illustrate the modeling of the microstrip using the cavity model, the principal E- and H-plane patterns have been computed at $f_0 = 10$ GHz for the rectangular microstrip of Example 14.1 with $\epsilon_r = 2.2$, $h = 0.1588$ cm, $L = 0.906$ cm and $L_e = 1.068$ cm. These are displayed in Figure 14.18(a) for the E-plane and Figure 14.18(b) for the H-plane where they are compared with measurements. A good agreement is indicated. However there are some differences in the E-plane primarily near grazing and in the region below the ground plane. The differences near grazing in the E-plane are primarily because the theory assumes the dielectric material of the substrate is truncated and does not cover the ground plane beyond the edges of the patch while those in the back region are because the theory assumes an infinite ground plane. The shape of the H-plane patterns are not affected significantly by the dielectric cover or the edges. Edge effects can be taken into account using diffraction theory [48], [79].

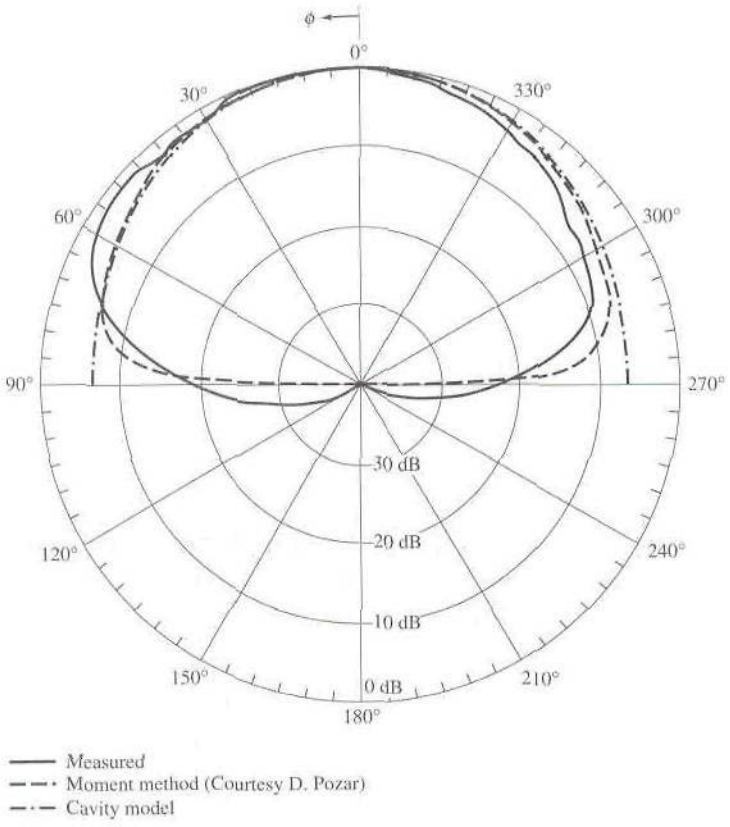

(a) E-plane ($\theta = 90°$)

Figure 14.18 Predicted and measured E- and H-plane patterns of rectangular microstrip patch ($L = 0.906$ cm, $W = 1.186$ cm, $h = 0.1588$ cm, $y_0 = 0.3126$ cm, $\epsilon_r = 2.2$, $f_0 = 10$ GHz).

The noted asymmetry in the measured and Moment Method computed patterns is due to the feed which is not symmetrically positioned along the E-plane. The Moment Method analysis accounts for the position of the feed, while the cavity model does not account for it. The pattern for $0° \leq \phi \leq 180°$ [left half in Figure 14.18(a)] corresponds to observation angles which lie on the same side of the patch as does the feed probe.

The presence of the dielectric-covered ground plane modifies the reflection coefficient, which influences the magnitude and phase of the image. This is similar to the ground effects discussed in Section 4.8 of Chapter 4. To account for the dielectric, the reflection coefficient for vertical polarization of $+1$ must be replaced by the reflection coefficient of (4-125) while the reflection coefficient for horizontal polarization of -1 must be replaced by the reflection coefficient of (4-129). Basically the introduction of the reflection coefficients of (4-125) and (4-129) to account for the dielectric cover of the ground plane is to modify the boundary conditions of the perfect conductor to one with an impedance surface. The result is for (4-125) to modify the shape of the pattern in the E-plane of the microstrip antenna, primarily for observation angles near grazing (near the ground plane), as was done in Figure 4.28 for the lossy earth. Similar changes are expected for the microstrip antenna. The changes in the pattern near grazing come from the fact that for the perfect conductor the reflection coefficient for vertical polarization is $+1$ for all observation angles.

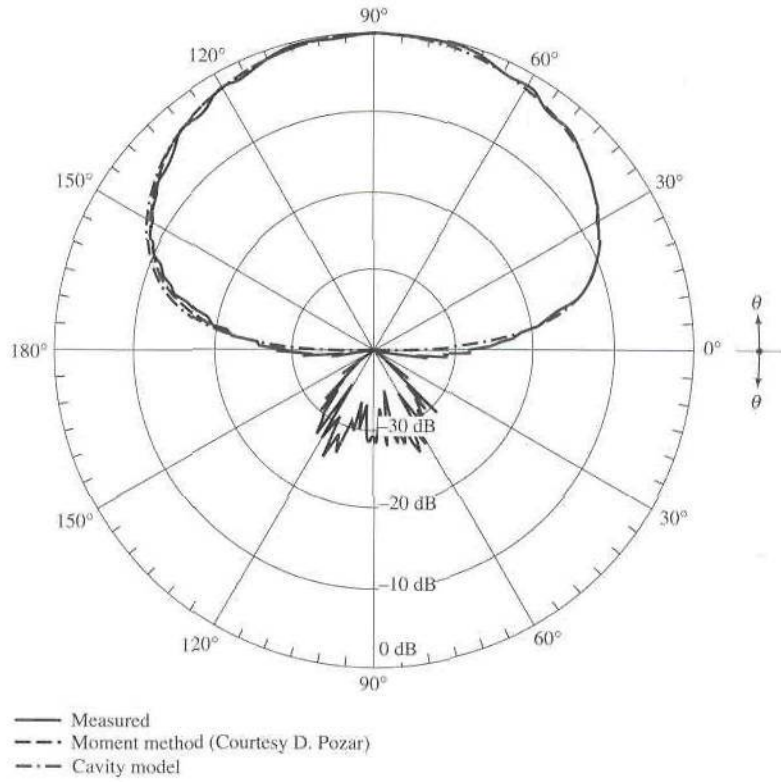

(b) H-plane ($\phi = 0°$)

Figure 14.18 (Continued)

However for the dielectric-covered ground plane (impedance surface), the reflection coefficient of (4-129) is nearly $+1$ for observation angles far away from grazing but begins to change very rapidly near grazing and becomes -1 at grazing [79]; thus the formation of an ideal null at grazing.

Similarly the reflection coefficient of (4-129) should basically control the pattern primarily in the H-plane. However, because the reflection coefficient for horizontal polarization for a perfect conductor is -1 for all observation angles while that of (4-129) for the dielectric covered ground plane is nearly -1 for all observation angles, the shape of the pattern in the H-plane is basically unaltered by the presence of the dielectric cover [79]. This is illustrated in Figure 4.30 for the earth. The pattern also exhibits a null along the ground plane. Similar changes are expected for the microstrip antenna.

Nonradiating Slots The fields radiated by the so-called nonradiating slots, each of effective length L_e and height h, are found using the same procedure as for the two radiating slots. Using the fields of (14-39), the equivalent magnetic current density of one of the nonradiating slots facing the $+z$ axis is

$$\mathbf{M}_s = -2\hat{\mathbf{n}} \times \mathbf{E}_a = \hat{\mathbf{a}}_y 2E_0 \cos\left(\frac{\pi}{L_e}y'\right) \tag{14-47}$$

and it is sketched in Figure 14.17. A similar one is facing the $-z$ axis. Using the same procedure as for the radiating slots, the normalized far-zone electric field components radiated by each slot are given by

$$E_\theta = -\frac{k_0 h L_e E_0 e^{-jk_0 r}}{2\pi r}\left\{Y\cos\phi\frac{\sin X}{X}\frac{\cos Y}{(Y)^2 - (\pi/2)^2}\right\}e^{j(X+Y)} \tag{14-48a}$$

$$E_\phi = \frac{k_0 h L_e E_0 e^{-jk_0 r}}{2\pi r}\left\{Y\cos\theta\sin\phi\frac{\sin X}{X}\frac{\cos Y}{(Y)^2 - (\pi/2)^2}\right\}e^{j(X+Y)} \tag{14-48b}$$

where

$$X = \frac{k_0 h}{2}\sin\theta\cos\phi \tag{14-48c}$$

$$Y = \frac{k_0 L_e}{2}\sin\theta\sin\phi \tag{14-48d}$$

Since the two nonradiating slots form an array of two elements, of the same magnitude but of opposite phase, separated along the z axis by a distance W, the array factor is

$$(AF)_z = 2j\sin\left(\frac{k_0 W}{2}\cos\theta\right) \tag{14-49}$$

Therefore the total far-zone electric field is given by the product of each of (14-48a) and (14-48b) with the array factor of (14-49).

In the H-plane ($\phi = 0°$, $0° \le \theta \le 180°$), (14-48a) and (14-48b) are zero because the fields radiated by each quarter cycle of each slot are cancelled by the fields radiated by the other quarter. Similarly in the E-plane ($\theta = 90°$, $0° \le \phi \le 90°$ and $270° \le \phi \le 360°$) the total fields are also zero because (14-49) vanishes. This implies that the fields radiated by each slot are cancelled by the fields radiated by the other. The nonradiation in the principal planes by these two slots was discussed earlier and demonstrated by the current densities in Figure 14.17. However, these two slots do radiate away from the principal planes, but their field intensity in these other planes

is small compared to that radiated by the two radiating slots such that it is usually neglected. Therefore they are referred to as *nonradiating* slots.

14.2.3 Directivity

As for every other antenna, the directivity is one of the most important figures-of-merit whose definition is given by (2-16a) or

$$D_0 = \frac{U_{\max}}{U_0} = \frac{4\pi U_{\max}}{P_{\text{rad}}} \tag{14-50}$$

Single Slot ($k_0 h \ll 1$) Using the electric field of (14-41), the maximum radiation intensity and radiated power can be written, respectively, as

$$U_{\max} = \frac{|V_0|^2}{2\eta_0 \pi^2}\left(\frac{\pi W}{\lambda_0}\right)^2 \tag{14-51}$$

$$P_{\text{rad}} = \frac{|V_0|^2}{2\eta_0 \pi}\int_0^{\pi}\left[\frac{\sin\left(\frac{k_0 W}{2}\cos\theta\right)}{\cos\theta}\right]^2 \sin^3\theta\, d\theta \tag{14-52}$$

Therefore, the directivity of a single slot can be expressed as

$$D_0 = \left(\frac{2\pi W}{\lambda_0}\right)^2 \frac{1}{I_1} \tag{14-53}$$

where

$$I_1 = \int_0^{\pi}\left[\frac{\sin\left(\frac{k_0 W}{2}\cos\theta\right)}{\cos\theta}\right]^2 \sin^3\theta\, d\theta$$

$$= \left[-2 + \cos(X) + XS_i(X) + \frac{\sin(X)}{X}\right] \tag{14-53a}$$

$$X = k_0 W \tag{14-53b}$$

Asymptotically the values of (14-53) vary as

$$D_0 = \begin{cases} 3.3 \text{ (dimensionless)} = 5.2 \text{ dB} & W \ll \lambda_0 \\ 4\left(\frac{W}{\lambda_0}\right) & W \gg \lambda_0 \end{cases} \tag{14-54}$$

The directivity of a single slot can be computed using (14-53) and (14-53a). In addition, it can also be computed using (14-41) and the computer program DIRECTIVITY at the end of Chapter 2. Since both are based on the same formulas, they should give the same results. Plots of the directivity of a single slot for $h = 0.01\lambda_0$ and $0.05\lambda_0$ as a function of the width of the slot are shown in Figure 14.19. It is evident that the directivity of a single slot is not influenced strongly by the height of the substrate, as long as it is maintained electrically small.

Two Slots ($k_0 h \ll 1$) For two slots, using (14-44), the directivity can be written as

$$D_2 = \left(\frac{2\pi W}{\lambda_0}\right)^2 \frac{\pi}{I_2} = \frac{2}{15 G_{\text{rad}}}\left(\frac{W}{\lambda_0}\right)^2 \tag{14-55}$$

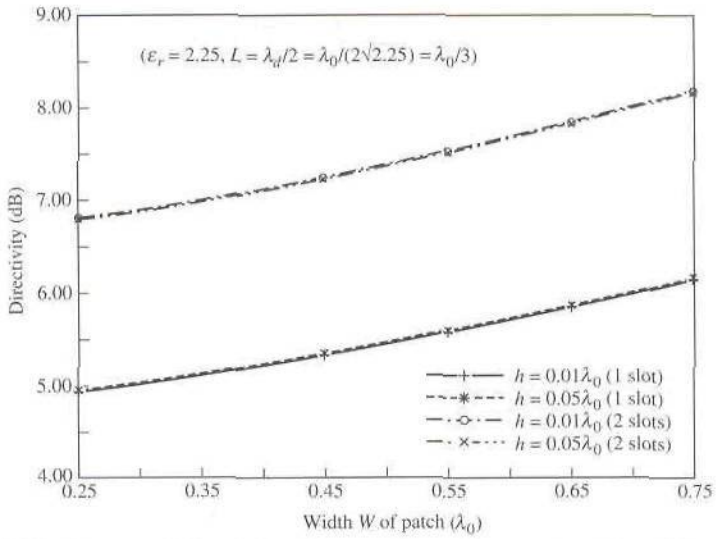

Figure 14.19 Computed directivity of one and two slots as a function of the slot width.

where G_{rad} is the radiation conductance and

$$I_2 = \int_0^{\pi}\int_0^{\pi}\left[\frac{\sin\left(\frac{k_0 W}{2}\cos\theta\right)}{\cos\theta}\right]^2 \sin^3\theta\cos^2\left(\frac{k_0 L_e}{2}\sin\theta\sin\phi\right)d\theta\,d\phi \qquad (14\text{-}55a)$$

The total broadside directivity D_2 for the two radiating slots, separated by the dominant TM^x_{010} mode field (antisymmetric voltage distribution), can also be written as [8], [82]

$$D_2 = D_0 D_{AF} = D_0\frac{2}{1+g_{12}} \qquad (14\text{-}56)$$

$$D_{AF} = \frac{2}{1+g_{12}} \overset{g_{12}\ll 1}{\simeq} 2 \qquad (14\text{-}56a)$$

where

D_0 = directivity of single slot [as given by (14-53) and (14-53a)]

D_{AF} = directivity of array factor AF

$$\left[AF = \cos\left(\frac{k_0 L_e}{2}\sin\theta\sin\phi\right)\right]$$

g_{12} = normalized mutual conductance = G_{12}/G_1

This can also be justified using the array theory of Chapter 6. The normalized mutual conductance g_{12} can be obtained using (14-12), (14-12a), and (14-18a). Computed values based on (14-18a) show that usually $g_{12} \ll 1$; thus (14-56a) is usually a good approximation to (14-56).

Asymptotically the directivity of two slots (microstrip antenna) can be expressed as

$$D_2 = \begin{cases} 6.6 \text{ (dimensionless)} = 8.2 \text{ dB} & W \ll \lambda_0 \\ 8\left(\dfrac{W}{\lambda_0}\right) & W \gg \lambda_0 \end{cases} \tag{14-57}$$

The directivity of the microstrip antenna can now be computed using (14-55) and (14-55a). In addition, it can also be computed using (14-44) and the computer program DIRECTIVITY at the end of Chapter 2. Since they are based on the same formulas, they should give the same results. Plots of directivity of a microstrip antenna, modeled by two slots, for $h = 0.01\,\lambda_0$ and $0.05\lambda_0$ are shown plotted as a function of the width of the patch (W/λ_0) in Figure 14.19. It is evident that the directivity is not a strong function of the height, as long as the height is maintained electrically small. A typical plot of the directivity of a patch for a fixed resonant frequency as a function of the substrate height (h/λ_0), for two different dielectrics, is shown in Figure 14.20.

The directivity of the slots also can be approximated by Kraus's, (2-26), and Tai & Pereira's, (2-30a), formulas in terms of the E- and H-plane beamwidths, which can be approximated by [36]

$$\Theta_E \simeq 2\cos^{-1}\sqrt{\frac{7.03\lambda_0^2}{4(3L_e^2 + h^2)\pi^2}} \tag{14-58}$$

$$\Theta_H \simeq 2\cos^{-1}\sqrt{\frac{1}{2 + k_0 W}} \tag{14-59}$$

The values of the directivities obtained using (14-58) and (14-59) along with either (2-26) or (2-30a) will not be very accurate since the beamwidths, especially in the E-plane, are very large. However, they can serve as guidelines.

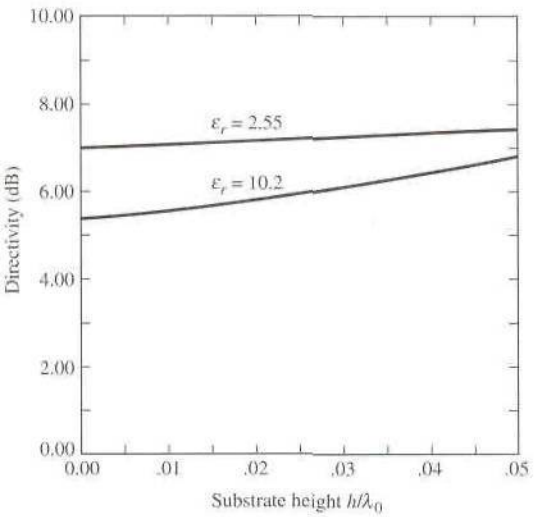

Figure 14.20 Directivity variations as a function of substrate height for a square microstrip patch antenna. (Courtesy of D. M. Pozar)

Example 14.3

For the rectangular microstrip antenna of Examples 14.1 and 14.2, with overall dimensions of $L = 0.906$ cm and $W = 1.186$ cm, substrate height $h = 0.1588$ cm, and dielectric constant of $\epsilon_r = 2.2$, center frequency of 10 GHz, find the directivity based on (14-56) and (14-56a). Compare with the values obtained using (14-55) and (14-55a).

SOLUTION

From the solution of Example 14.2

$$G_1 = 0.00157 \text{ Siemens}$$

$$G_{12} = 6.1683 \times 10^{-4} \text{ Siemens}$$

$$g_{12} = G_{12}/G_1 = 0.3921$$

Using (14-56a)

$$D_{AF} = \frac{2}{1 + g_{12}} = \frac{2}{1 + 0.3921} = 1.4367 = 1.5736 \text{ dB}$$

Using (14-53) and (14-53a)

$$I_1 = 1.863$$

$$D_0 = \left(\frac{2\pi W}{\lambda_0}\right)^2 \frac{1}{I_1} = 3.312 = 5.201 \text{ dB}$$

According to (14-56)

$$D_2 = D_0 D_{AF} = 3.312(1.4367) = 4.7584 = 6.7746 \text{ dB}$$

Using (14-55a)

$$I_2 = 3.59801$$

Finally, using (14-55)

$$D_2 = \left(\frac{2\pi W}{\lambda_0}\right)^2 \frac{\pi}{I_2} = 5.3873 = 7.314 \text{ dB}$$

14.3 CIRCULAR PATCH

Other than the rectangular patch, the next most popular configuration is the circular patch or disk, as shown in Figure 14.21. It also has received a lot of attention not only as a single element [6], [10], [13], [46], [47], [51], but also in arrays [65] and [74]. The modes supported by the circular patch antenna can be found by treating the patch, ground plane, and the material between the two as a circular cavity. As with the rectangular patch, the modes that are supported primarily by a circular microstrip antenna whose substrate height is small ($h \ll \lambda$) are TM^z where z is taken perpendicular to the patch. As far as the dimensions of the patch, there are two degrees of freedom to control (length and width) for the rectangular microstrip antenna. Therefore the order of the modes can be changed by changing the relative dimensions of the width and length of the patch (width-to-length ratio). However, for the circular patch

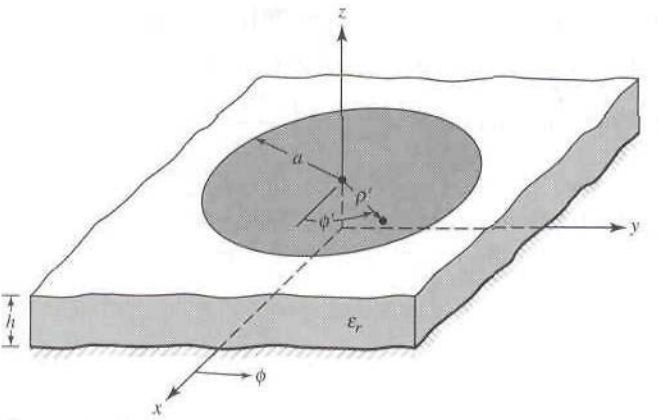

Figure 14.21 Geometry of circular microstrip patch antenna.

there is only one degree of freedom to control (radius of the patch). Doing this does not change the order of the modes; however, it does change the absolute value of the resonant frequency of each [79].

Other than using full-wave analysis [51], [65], [74], the circular patch antenna can only be analyzed conveniently using the cavity model [10], [46], [47]. This can be accomplished using a procedure similar to that for the rectangular patch but now using cylindrical coordinates [79]. The cavity is composed of two perfect electric conductors at the top and bottom to represent the patch and the ground plane, and by a cylindrical perfect magnetic conductor around the circular periphery of the cavity. The dielectric material of the substrate is assumed to be truncated beyond the extent of the patch.

14.3.1 Electric and Magnetic Fields—TM^z_{mnp}

To find the fields within the cavity, we use the vector potential approach. For TM^z we need to first find the magnetic vector potential A_z, which must satisfy, in cylindrical coordinates, the homogeneous wave equation of

$$\nabla^2 A_z(\rho, \phi, z) + k^2 A_z(\rho, \phi, z) = 0. \tag{14-60}$$

It can be shown that for TM^z modes, whose electric and magnetic fields are related to the vector potential A_z by [79]

$$\begin{aligned} E_\rho &= -j\frac{1}{\omega\mu\epsilon}\frac{\partial^2 A_z}{\partial\rho\partial z} & H_\rho &= \frac{1}{\mu}\frac{1}{\rho}\frac{\partial A_z}{\partial\phi} \\ E_\phi &= -j\frac{1}{\omega\mu\epsilon}\frac{1}{\rho}\frac{\partial^2 A_z}{\partial\phi\partial z} & H_\phi &= -\frac{1}{\mu}\frac{\partial A_z}{\partial\rho} \\ E_z &= -j\frac{1}{\omega\mu\epsilon}\left(\frac{\partial^2}{\partial z^2} + k^2\right)A_z & H_z &= 0 \end{aligned} \tag{14-61}$$

subject to the boundary conditions of

$$\begin{aligned} E_\rho(0 \le \rho' \le a, 0 \le \phi' \le 2\pi, z' = 0) &= 0 \\ E_\rho(0 \le \rho' \le a, 0 \le \phi' \le 2\pi, z' = h) &= 0 \\ H_\phi(\rho' = a, 0 \le \phi' \le 2\pi, 0 \le z' \le h) &= 0 \end{aligned} \tag{14-62}$$

the magnetic vector potential A_z reduces to [79]

$$A_z = B_{mnp} J_m(k_\rho \rho')[A_2 \cos(m\phi') + B_2 \sin(m\phi')] \cos(k_z z') \tag{14-63}$$

with the constraint equation of

$$(k_\rho)^2 + (k_z)^2 = k_r^2 = \omega_r^2 \mu\epsilon \tag{14-63a}$$

The primed cylindrical coordinates ρ', ϕ', z' are used to represent the fields within the cavity while $J_m(x)$ is the Bessel function of the first kind of order m, and

$$k_\rho = \chi'_{mn}/a \tag{14-63b}$$

$$k_z = \frac{p\pi}{h} \tag{14-63c}$$

$$m = 0, 1, 2, \ldots \tag{14-63d}$$

$$n = 1, 2, 3, \ldots \tag{14-63e}$$

$$p = 0, 1, 2, \ldots \tag{14-63f}$$

In (14-63b) χ'_{mn} represents the zeroes of the derivative of the Bessel function $J_m(x)$, and they determine the order of the resonant frequencies. The first four values of χ'_{mn}, in ascending order, are

$$\begin{aligned} \chi'_{11} &= 1.8412 \\ \chi'_{21} &= 3.0542 \\ \chi'_{01} &= 3.8318 \\ \chi'_{31} &= 4.2012 \end{aligned} \tag{14-64}$$

14.3.2 Resonant Frequencies

The resonant frequencies of the cavity, and thus of the microstrip antenna, are found using (14-63a)–(14-63f). Since for most typical microstrip antennas the substrate height h is very small (typically $h < 0.05\lambda_0$), the fields along z are essentially constant and are presented in (14-63f) by $p = 0$ and in (14-63c) by $k_z = 0$. Therefore the resonant frequencies for the TM^z_{mn0} modes can be written using (14-63a) as

$$(f_r)_{mn0} = \frac{1}{2\pi\sqrt{\mu\epsilon}} \left(\frac{\chi'_{mn}}{a}\right) \tag{14-65}$$

Based on the values of (14-64), the first four modes, in ascending order, are TM^z_{110}, TM^z_{210}, TM^z_{010}, and TM^z_{310}. The dominant mode is the TM^z_{110} whose resonant frequency is

$$(f_r)_{110} = \frac{1.8412}{2\pi a\sqrt{\mu\epsilon}} = \frac{1.8412 v_0}{2\pi a\sqrt{\epsilon_r}} \tag{14-66}$$

where v_0 is the speed of light in free space.

The resonant frequency of (14-66) does not take into account fringing. As was shown for the rectangular patch, and illustrated in Figure 14.7, fringing makes the patch look electrically larger and it was taken into account by introducing a length correction factor given by (14-2). Similarly for the circular patch a correction is

introduced by using an effective radius a_e, to replace the actual radius a, given by [6]

$$a_e = a\left\{1 + \frac{2h}{\pi a \epsilon_r}\left[\ln\left(\frac{\pi a}{2h}\right) + 1.7726\right]\right\}^{1/2} \tag{14-67}$$

Therefore the resonant frequency of (14-66) for the dominant TM_{110}^z should be modified by using (14-67) and expressed as

$$(f_r)_{110} = \frac{1.8412 v_0}{2\pi a_e \sqrt{\epsilon_r}} \tag{14-68}$$

14.3.3 Design

Based on the cavity model formulation, a design procedure is outlined which leads to practical designs of circular microstrip antennas for the dominant TM_{110}^z mode. The procedure assumes that the specified information includes the dielectric constant of the substrate (ϵ_r), the resonant frequency (f_r) and the height of the substrate h. The procedure is as follows:

Specify

$$\epsilon_r, f_r(\text{in Hz}), \text{ and } h \text{ (in cm)}$$

Determine The actual radius a of the patch.

Design Procedure A first-order approximation to the solution of (14-67) for a is to find a_e using (14-68) and to substitute that into (14-67) for a_e and for a in the logarithmic function. Doing this leads to

$$a = \frac{F}{\left\{1 + \frac{2h}{\pi \epsilon_r F}\left[\ln\left(\frac{\pi F}{2h}\right) + 1.7726\right]\right\}^{1/2}} \tag{14-69}$$

where

$$F = \frac{8.791 \times 10^9}{f_r \sqrt{\epsilon_r}} \tag{14-69a}$$

Remember that h *in (14-69) must be in cm.*

Example 14.4

Design a circular microstrip antenna using a substrate (RT/duroid 5880) with a dielectric constant of 2.2, $h = 0.1588$ cm (0.0625 in.) so as to resonate at 10 GHz.

SOLUTION

Using (14-69a)

$$F = \frac{8.791 \times 10^9}{10 \times 10^9 \sqrt{2.2}} = 0.593$$

Therefore using (14-69)

$$a = \frac{F}{\left\{1 + \frac{2h}{\pi\epsilon_r F}\left[\ln\left(\frac{\pi F}{2h}\right) + 1.7726\right]\right\}^{1/2}} = 0.525 \text{ cm } (0.207 \text{ in.})$$

14.3.4 Equivalent Current Densities and Fields Radiated

As was done for the rectangular patch using the cavity model, the fields radiated by the circular patch can be found by using the Equivalence Principle whereby the circumferential wall of the cavity is replaced by an equivalent magnetic current density of (14-38) as shown in Figure 14.22. Based on (14-61)–(14-63) and assuming a TM_{110}^{z} mode field distribution beneath the patch, the normalized electric and magnetic fields within the cavity for the cosine azimuthal variations can be written as

$$E_\rho = E_\phi = H_z = 0 \tag{14-70a}$$

$$E_z = E_0 J_1(k\rho') \cos\phi' \tag{14-70b}$$

$$H_\rho = j\frac{E_0}{\omega\mu_0}\frac{1}{\rho} J_1(k\rho') \sin\phi' \tag{14-70c}$$

$$H_\phi = j\frac{E_0}{\omega\mu_0} J_1'(k\rho') \cos\phi' \tag{14-70d}$$

where $' = \partial/\partial\rho$ and ϕ' is the azimuthal angle along the perimeter of the patch.

Based on (14-70b) evaluated at the electrical equivalent edge of the disk ($\rho' = a_e$), the magnetic current density of (14-38) can be written as

$$\mathbf{M}_s = -2\hat{\mathbf{n}} \times \mathbf{E}_a|_{\rho'=a_e} = \hat{\mathbf{a}}_\phi 2E_0 J_1(ka_e) \cos\phi' \tag{14-71}$$

Since the height of the substrate is very small and the current density of (14-71) is uniform along the z direction, we can approximate (14-71) by a filamentary magnetic current of

$$\mathbf{I}_m = h\mathbf{M}_s = \hat{\mathbf{a}}_\phi 2hE_0 J_1(ka_e) \cos\phi' = \hat{\mathbf{a}}_\phi 2V_0 \cos\phi' \tag{14-71a}$$

where $V_0 = hE_0 J_1(ka_e)$ at $\phi' = 0$.

Using (14-71a) the microstrip antenna can be treated as a circular loop. Referring to Chapter 5 for the loop and using the radiation equations of Sections 12.3 and 12.6, we can write that [10], [83]

$$E_r = 0 \tag{14-72a}$$

$$E_\theta = -j\frac{k_0 a_e V_0 e^{-jk_0 r}}{2r}\{\cos\phi J_{02}'\} \tag{14-72b}$$

$$E_\phi = j\frac{k_0 a_e V_0 e^{-jk_0 r}}{2r}\{\cos\theta \sin\phi J_{02}\} \tag{14-72c}$$

$$J_{02}' = J_0(k_0 a_e \sin\theta) - J_2(k_0 a_e \sin\theta) \tag{14-72d}$$

$$J_{02} = J_0(k_0 a_e \sin\theta) + J_2(k_0 a_e \sin\theta) \tag{14-72e}$$

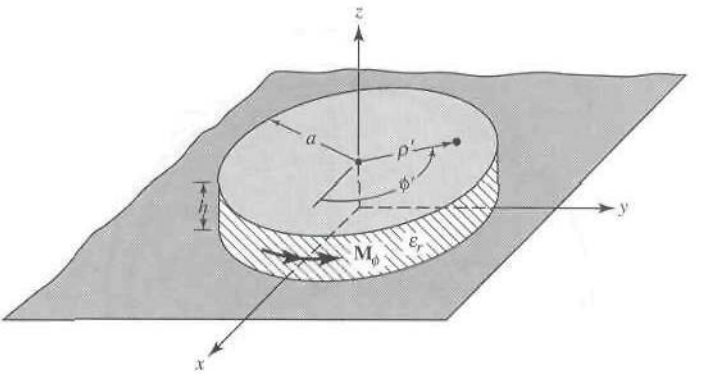

Figure 14.22 Cavity model and equivalent magnetic current density for circular microstrip patch antenna.

where a_e is the effective radius as given by (14-67). The fields in the principal planes reduce to:

$$\textbf{E-plane } (\phi = 0°, 180°, 0° \leq \theta \leq 90°)$$

$$E_\theta = j\frac{k_0 a_e V_0 e^{-jk_0 r}}{2r}[J'_{02}] \tag{14-73a}$$

$$E_\phi = 0 \tag{14-73b}$$

$$\textbf{H-plane } (\phi = 90°, 270°, 0° \leq \theta \leq 90°)$$

$$E_\theta = 0 \tag{14-74a}$$

$$E_\phi = j\frac{k_0 a_e V_0 e^{-jk_0 r}}{2r}[\cos\theta\, J_{02}] \tag{14-74b}$$

Patterns have been computed for the circular patch of Example 14.4 based on (14-73a)–(14-74b), and they are shown in Figure 14.23 where they are compared with measurements and Moment Method computed patterns. The noted asymmetry in the measured and Moment Method computed patterns is due to the feed which is not symmetrically positioned along the E-plane. The Moment Method analysis accounts for the position of the feed, while the cavity model does not account for it. The pattern for the left half of Figure 14.23(a) corresponds to observation angles which lie on the same side of the patch as does the feed probe.

14.3.5 Conductance and Directivity

The conductance due to the radiated power and directivity of the circular microstrip patch antenna can be computed using their respective definitions of (14-10) and (14-50). For each we need the radiated power, which based on the fields of (14-72b) and (14-72c) of the cavity model can be expressed as

$$P_{\text{rad}} = |V_0|^2 \frac{(k_0 a_e)^2}{960}\int_0^{\pi/2}[J'^2_{02} + \cos^2\theta\, J^2_{02}]\sin\theta\, d\theta \tag{14-75}$$

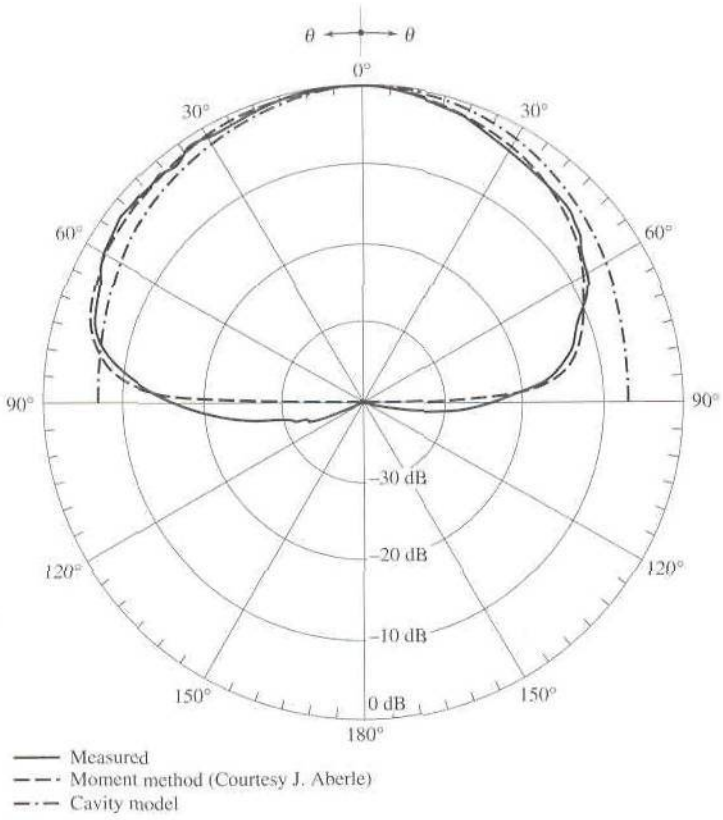

(a) E-plane ($\phi = 0°, 180°$)

Figure 14.23 Measured and computed (based on moment method and cavity models) E- and H-plane patterns of circular microstrip patch antenna ($a = 0.525$ cm, $a_e = 0.598$ cm, $\rho_f = 0.1$ cm, $\epsilon_r = 2.2$, $h = 0.1588$ cm, $f_0 = 10$ GHz, $\lambda_0 = 3$ cm).

Therefore the conductance across the gap between the patch and the ground plane at $\phi' = 0°$ based on (14-10) and (14-75) can be written as

$$G_{\text{rad}} = \frac{(k_0 a_e)^2}{480} \int_0^{\pi/2} [J_{02}'^2 + \cos^2\theta\, J_{02}^2] \sin\theta\, d\theta \tag{14-76}$$

A plot of the conductance of (14-76) for the TM_{110}^z mode is shown in Figure 14.24. While the conductance of (14-76) accounts for the losses due to radiation, it does not take into account losses due to conduction (ohmic) and dielectric losses, which each can be expressed as [10]

$$G_c = \frac{\epsilon_{mo}\pi(\pi\mu_0 f_r)^{-3/2}}{4h^2\sqrt{\sigma}}[(ka_e)^2 - m^2] \tag{14-77}$$

$$G_d = \frac{\epsilon_{mo}\tan\delta}{4\mu_0 h f_r}[(ka_e)^2 - m^2] \tag{14-78}$$

where $\epsilon_{mo} = 2$ for $m = 0$, $\epsilon_{mo} = 1$ for $m \neq 0$, and f_r represents the resonant frequency of the $mn0$ mode. Thus, the total conductance can be written as

$$G_t = G_{\text{rad}} + G_c + G_d \tag{14-79}$$

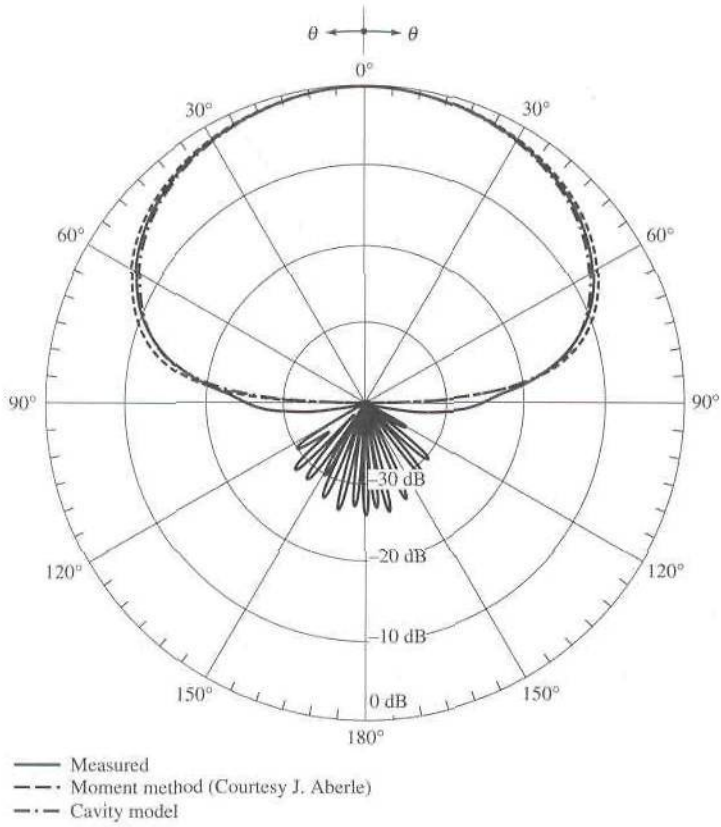

(a) H-plane ($\phi = 90°, 270°$)

Figure 14.23 (continued)

Based on (14-50), (14-72b), (14-72c), (14-75) and (14-76), the directivity for the slot at $\theta = 0°$ can be expressed as

$$D_0 = \frac{(k_0 a_e)^2}{120 G_{\text{rad}}} \tag{14-80}$$

A plot of the directivity of the dominant TM^z_{110} mode as a function of the radius of the disk is shown plotted in Figure 14.25. For very small values of the radius the directivity approaches 3 (4.8 dB), which is equivalent of that of a slot above a ground plane and it agrees with the value of (14-54) for $W \ll \lambda_0$.

14.3.6 Resonant Input Resistance

As was the case for the rectangular patch antenna, the input impedance of a circular patch at resonance is real. The input power is independent of the feed point position along the circumference. Taken the reference of the feed at $\phi' = 0°$, the input resistance at any radial distance $\rho' = \rho_0$ from the center of the patch can be written as

$$R_{\text{in}}(\rho' = \rho_0) = \frac{1}{G_t} \frac{J_m^2(k\rho_0)}{J_m^2(ka_e)} \tag{14-81}$$

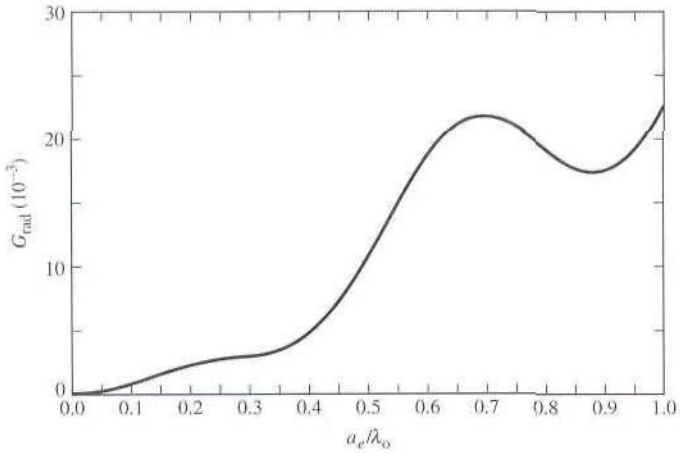

Figure 14.24 Radiation conductance versus effective radius for circular microstrip patch operating in dominant TM^z_{110} mode.

where G_t is the total conductance due to radiation, conduction (ohmic) and dielectric losses, as given by (14-79). As was the case with the rectangular patch, the resonant input resistance of a circular patch with an inset feed, which is usually a probe, can be written as

$$R_{in}(\rho' = \rho_0) = R_{in}(\rho' = a_e)\frac{J_m^2(k\rho_0)}{J_m^2(ka_e)} \tag{14-82}$$

where

$$R_{in}(\rho' = a_e) = \frac{1}{G_t} \tag{14-82a}$$

This is analogous to (14-20a) for the rectangular patch.

14.4 QUALITY FACTOR, BANDWIDTH AND EFFICIENCY

The quality factor, bandwidth, and efficiency are antenna figures-of-merit, which are interrelated, and there is no complete freedom to independently optimize each one. Therefore there is always a tradeoff between them in arriving at an optimum antenna performance. Often, however, there is a desire to optimize one of them while reducing the performance of the other.

The quality factor is a figure-of-merit that is representative of the antenna losses. Typically there are radiation, conduction (ohmic), dielectric and surface wave losses. Therefore the total quality factor Q_t is influenced by all of these losses and is, in general, written as [16]

$$\frac{1}{Q_t} = \frac{1}{Q_{rad}} + \frac{1}{Q_c} + \frac{1}{Q_d} + \frac{1}{Q_{sw}} \tag{14-83}$$

where

Q_t = total quality factor

Q_{rad} = quality factor due to radiation (space wave) losses

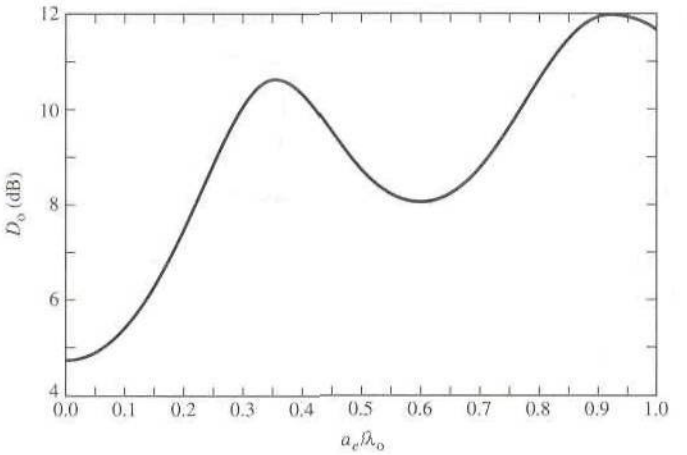

Figure 14.25 Directivity versus effective radius for circular microstrip patch antenna operating in dominant TM^z_{110} mode.

Q_c = quality factor due to conduction (ohmic) losses

Q_d = quality factor due to dielectric losses

Q_{sw} = quality factor due to surface waves

For very thin substrates, the losses due to surface waves are very small and can be neglected. However, for thicker substrates they need to be taken into account [84]. These losses can also be eliminated by using cavities [50] and [51].

For very thin substrates ($h \ll \lambda_0$) of arbitrary shapes (including rectangular and circular), there are approximate formulas to represent the quality factors of the various losses [16], [85]. These can be expressed as

$$Q_c = h\sqrt{\pi f \mu \sigma} \tag{14-84}$$

$$Q_d = \frac{1}{\tan \delta} \tag{14-85}$$

$$Q_{\text{rad}} = \frac{2\omega\epsilon_r}{hG_t/l} K \tag{14-86}$$

where $\tan \delta$ is the loss tangent of the substrate material, σ is the conductivity of the conductors associated with the patch and ground plane, G_t/l is the total conductance per unit length of the radiating aperture and

$$K = \frac{\iint_{\text{area}} |E|^2 \, dA}{\oint_{\text{perimeter}} |E|^2 \, dl} \tag{14-86a}$$

For a rectangular aperture operating in the dominant TM^x_{010} mode

$$K = \frac{L}{4} \tag{14-87a}$$

$$G_{t/l} = \frac{G_{\text{rad}}}{W} \tag{14-87b}$$

The Q_{rad} as represented by (14-86) is inversely proportional to the height of the substrate, and for very thin substrates is usually the dominant factor.

The fractional bandwidth of the antenna is inversely proportional to the Q_t of the antenna, and it is defined by (11-36) or

$$\frac{\Delta f}{f_0} = \frac{1}{Q_t} \tag{14-88}$$

However, (14-88) may not be as useful because it does not take into account impedance matching at the input terminals of the antenna. A more meaningful definition of the fractional bandwidth is over a band of frequencies where the VSWR at the input terminals is equal to or less than a desired maximum value, assuming that the VSWR is unity at the design frequency. A modified form of (14-88) that takes into account the impedance matching is [16]

$$\frac{\Delta f}{f_0} = \frac{\text{VSWR} - 1}{Q_t\sqrt{\text{VSWR}}} \tag{14-88a}$$

In general it is proportional to the volume, which for a rectangular microstrip antenna at a constant resonant frequency can be expressed as

$$\text{BW} \sim \text{volume} = \text{area} \cdot \text{height} = \text{length} \cdot \text{width} \cdot \text{height}$$

$$\sim \frac{1}{\sqrt{\epsilon_r}} \frac{1}{\sqrt{\epsilon_r}} \sqrt{\epsilon_r} = \frac{1}{\sqrt{\epsilon_r}} \tag{14-89}$$

Therefore the bandwidth is inversely proportional to the square root of the dielectric constant of the substrate. A typical variation of the bandwidth for a microstrip antenna as a function of the normalized height of the substrate, for two different substrates, is shown in Figure 14.26. It is evident that the bandwidth increases as the substrate height increases.

The radiation efficiency of an antenna is expressed by (2-90), and it is defined as the power radiated over the input power. It can also be expressed in terms of the quality factors, which for a microstrip antenna can be written as

$$e_{cdsw} = \frac{1/Q_{\text{rad}}}{1/Q_t} = \frac{Q_t}{Q_{\text{rad}}} \tag{14-90}$$

where Q_t is given by (14-83). Typical variations of the efficiency as a function of the substrate height for a microstrip antenna, with two different substrates, are shown in Figure 14.26.

14.5 INPUT IMPEDANCE

In the previous sections of this chapter, we derived approximate expressions for the resonant input resistance for both rectangular and circular microstrip antennas. Also, approximate expressions were stated which describe the variation of the resonant input resistance as a function of the inset feed position, which can be used effectively to match the antenna element to the input transmission line. In general, the input impedance is complex and it includes both a resonant and a nonresonant part which is usually reactive. Both the real and imaginary parts of the impedance vary as a function of frequency, and a typical variation is shown in Figure 14.27. Ideally both the resistance and reactance exhibit symmetry about the resonant frequency, and the reactance at resonance is equal to the average of sum of its maximum value (which is positive) and its minimum value (which is negative).

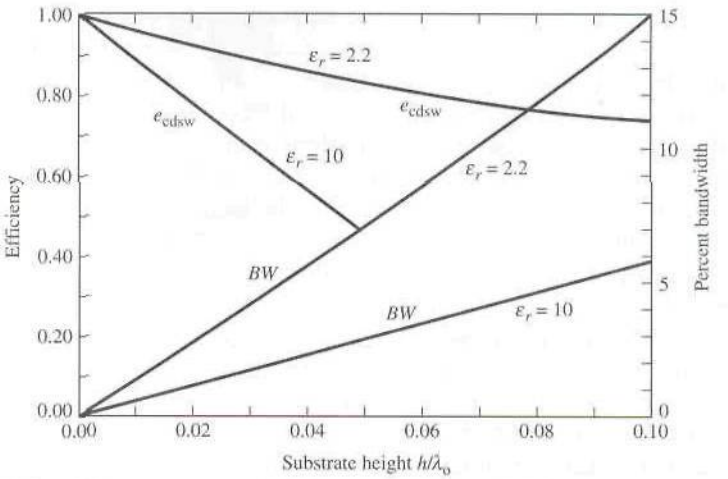

Figure 14.26 Efficiency and bandwidth versus substrate height at constant resonant frequency for rectangular microstrip patch for two different substrates (SOURCE: D. M. Pozar, "Microstrip Antennas," *Proc. IEEE*, Vol. 80, No. 1, January 1992. © 1992 IEEE).

Typically the feed reactance is very small, compared to the resonant resistance, for very thin substrates. However, for thick elements the reactance may be significant and needs to be taken into account in impedance matching and in determining the resonant frequency of a loaded element [34]. The variations of the feed reactance as a function of position can be intuitively explained by considering the cavity model for a rectangular patch with its four side perfect magnetic conducting walls [34], [85].

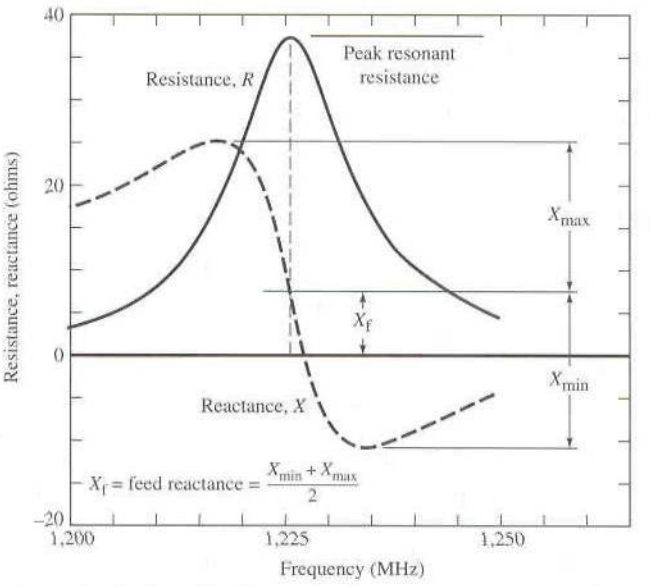

Figure 14.27 Typical variation of resistance and reactance of rectangular microstrip antenna versus frequency (*Electromagnetics*, Vol. 3, Nos. 3 and 4, p. 33, W. F. Richards, J. R. Zinecker, and R. D. Clark, Taylor & Francis, Washington, D.C. Reproduced by permission. All rights reserved).

As far as the impedance is concerned, the magnetic walls can be taken into account by introducing multiple images with current flow in the same direction as the actual feed. When the feed point is far away from one of the edges, the magnetic field associated with the images and that of the actual feed do not overlap strongly. Therefore the inductance associated with the magnetic energy density stored within a small testing volume near the feed will be primarily due to the current of the actual feed. However, when the feed is at one of the edges, the feed and one of the images, which accounts for the magnetic wall at that edge, coincide. Thus, the associated magnetic field stored energy of the equivalent circuit doubles while the respective stored magnetic energy density quadruples. However, because the volume in the testing region of the patch is only half from that when the feed was far removed from the edge, the net stored magnetic density is only double of that of the feed alone. Thus, the associated inductance and reactance, when the feed is at the edge, is twice that when the feed is far removed from the edge. When the feed is at a corner, there will be three images in the testing volume of the patch, in addition to the actual feed, to take into account the edges that form the corner. Using the same argument as above, the associated inductance and reactance for a feed at a corner is four times that when the feed is removed from an edge or a corner. Thus, the largest reactance (about a factor of four larger) is when the feed is at or near a corner while the smallest is when the feed is far removed from an edge or a corner.

Although such an argument predicts the relative variations (trends) of the reactance as a function of position, they do predict very accurately the absolute values especially when the feed is at or very near an edge. In fact it overestimates the values for feeds right on the edge; the actual values predicted by the cavity model with perfect magnetic conducting walls are smaller [34]. A formula that has been suggested to approximate the feed reactance, which does not take into account any images, is

$$x_f \simeq -\frac{\eta kh}{2\pi}\left[\ln\left(\frac{kd}{4}\right) + 0.577\right] \tag{14-91}$$

where d is the diameter of the feed probe. More accurate predictions of the input impedance, based on full wave models, have been made for circular patches where an attachment current mode is introduced to match the current distribution of the probe to that of the patch [74].

14.6 COUPLING

The coupling between two or more microstrip antenna elements can be taken into account easily using full-wave analyses. However, it is more difficult to do using the transmission-line and cavity models, although successful attempts have been made using the transmission-line model [75] and the cavity model [76], [77]. It can be shown that coupling between two patches, as is coupling between two aperture or two wire antennas, is a function of the position of one element relative to the other. This has been demonstrated in Figures 4.20 for a vertical half-wavelength dipole above a ground plane and in Figure 4.27 for a horizontal half-wavelength dipole above a ground plane. From these two, the ground effects are more pronounced for the horizontal dipole. Also, mutual effects have been discussed in Chapter 8 for the three different arrangements of dipoles, as shown in Figure 8.20 whose side-by-side arrangement exhibits the largest variations of mutual impedance.

For two rectangular microstrip patches the coupling for two side-by-side elements is a function of the relative alignment. When the elements are positioned collinearly

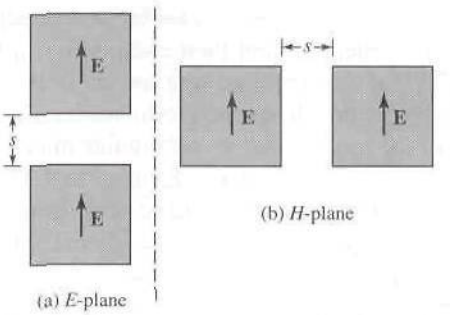

Figure 14.28 E- and H-plane arrangements of microstrip patch antennas.

along the E-plane, this arrangement is referred to as the *E-plane*, as shown in Figure 14.28(a); when the elements are positioned collinearly along the H-plane, this arrangement is referred to as the *H-plane*, as shown in Figure 14.28(b). For an edge-to-edge separation of s, the E-plane exhibits the smallest coupling isolation for very small spacing (typically $s < 0.10\lambda_0$) while the H-plane exhibits the smallest coupling for large spacing (typically $s > 0.10\lambda_0$). The spacing at which one plane coupling overtakes the other one depends on the electrical properties and geometrical dimensions of the microstrip antenna. Typical variations are shown in Figure 14.29.

In general, mutual coupling is primarily attributed to the fields that exist along the air-dielectric interface. The fields can be decomposed to space waves (with $1/\rho$ radial variations), higher order waves (with $1/\rho^2$ radial variations), surface waves (with $1/\rho^{1/2}$ radial variations), and leaky waves [with $\exp(-\lambda\rho)/\rho^{1/2}$ radial variations] [23], [86]. Because of the spherical radial variation, space ($1/\rho$) and higher order waves ($1/\rho^2$) are most dominant for very small spacing while surface waves, because

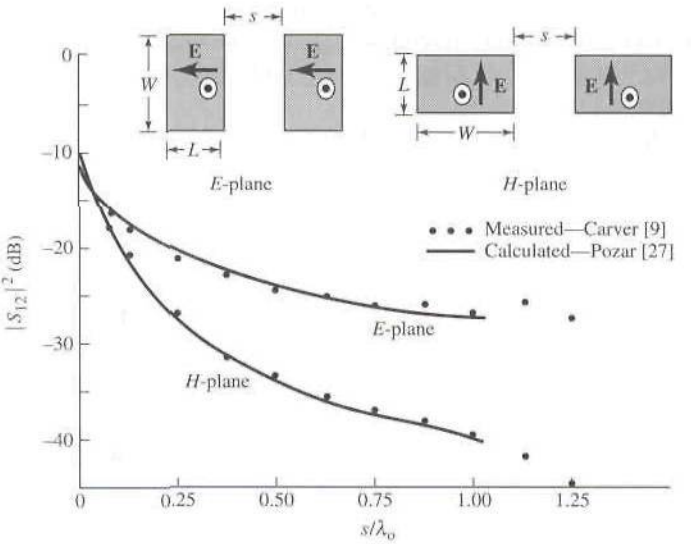

Figure 14.29 Measured and calculated mutual coupling between two coax-fed microstrip antennas, for both E-plane and H-plane coupling, ($W = 10.57$ cm, $L = 6.55$ cm, $h = 0.1588$ cm, $\epsilon_r = 2.55$, $f_r = 1{,}410$ MHz). (SOURCE: D. M. Pozar, "Input Impedance and Mutual Coupling of Rectangular Microstrip Antennas," *IEEE Trans. Antennas Propagat.*, Vol. AP-30, No. 6, November 1982. © 1982 IEEE)

of their $1/\rho^{1/2}$ radial variations are dominant for large separations. Surface waves exist and propagate within the dielectric, and their excitation is a function of the thickness of the substrate [79]. In a given direction, the lowest order (dominant) surface wave mode is TM(odd) with zero cutoff frequency followed by a TE(even), and alternatively by TM(odd) and TE(even) modes. For a rectangular microstrip patch, the fields are TM in a direction of progagation along the E-plane and TE in a direction of propagation along the H-plane. Since for the E-plane arrangement of Figure 14.28(a) the elements are placed collinearly along the E-plane where the fields in the space between the elements are primarily TM, there is a stronger surface wave excitation (based on a single dominant surface wave mode) between the elements, and the coupling is larger. However for the H-plane arrangement of Figure 14.28(b), the fields in the space between the elements are primarily TE and there is not as a strong dominant mode surface wave excitation; therefore there is less coupling between the elements. This does change as the thickness of the substrate increases which allows higher order TE surface wave excitation.

The mutual conductance between two rectangular microstrip patches has also been found using the basic definition of conductance given by (14-18), the far fields based on the cavity model, and the array theory of Chapter 6. For the E-plane arrangement of Figure 14.28(a) and for the odd mode field distribution beneath the patch, which is representative of the dominant mode, the mutual conductance is [8]

$$G_{12} = \frac{1}{\pi}\sqrt{\frac{\epsilon}{\mu}}\int_0^{\pi}\left[\frac{\sin\left(\frac{k_0 W}{2}\cos\theta\right)}{\cos\theta}\right]^2 \sin^3\theta\left\{2J_0\left(\frac{Y}{\lambda_0}2\pi\sin\theta\right)\right.$$
$$\left. + J_0\left(\frac{Y+L}{\lambda_0}2\pi\sin\theta\right) + J_0\left(\frac{Y-L}{\lambda_0}2\pi\sin\theta\right)\right\}d\theta \qquad (14\text{-}92)$$

where Y is the center-to-center separation between the slots and J_0 is the Bessel function of the first kind of order zero. The first term in (14-92) represents the mutual conductance of two slots separated by a distance X along the E-plane while the second and third terms represent, respectively, the conductances of two slots separated along the E-plane by distances $Y + L$ and $Y - L$. Typical normalized results are shown by the solid curve in Figure 14.30.

For the H-plane arrangement of Figure 14.28(b) and for the odd mode field distribution beneath the patch, which is representative of the dominant mode, the mutual conductance is [8]

$$G_{12} = \frac{2}{\pi}\sqrt{\frac{\epsilon}{\mu}}\int_0^{\pi}\left[\frac{\sin\left(\frac{k_0 W}{2}\cos\theta\right)}{\cos\theta}\right]^2 \sin^3\theta\cos\left(\frac{Z}{\lambda_0}2\pi\cos\theta\right)$$
$$\cdot\left\{1 + J_0\left(\frac{L}{\lambda_0}2\pi\sin\theta\right)\right\}d\theta \qquad (14\text{-}93)$$

where Z is the center-to-center separation between the slots and J_0 is the Bessel function of the first kind of order zero. The first term in (14-93) represents twice the mutual conductance of two slots separated along the H-plane by a distance Z while the second term represents twice the conductance between two slots separated along the E-plane by a distance L and along the H-plane by a distance Z. Typical normalized results are shown by the dotted curve in Figure 14.30. By comparing the results of Figures 14.30 it is clear that the mutual conductance for the H-plane arrangement, as expected, decreases with distance faster than that of the E-plane. Also it is observed

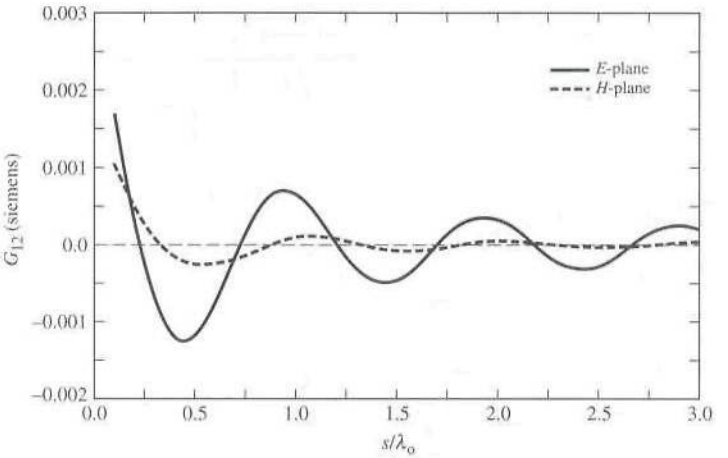

Figure 14.30 *E*- and *H*-plane mutual conductance versus patch separation for rectangular microstrip patch antennas ($W = 1.186$ cm, $L = 0.906$ cm, $\epsilon_r = 2.2$, $\lambda_0 = 3$ cm).

that the mutual conductance for the *E*-plane arrangement is higher for wider elements while it is lower for wider elements for the *H*-plane arrangement.

14.7 CIRCULAR POLARIZATION

The patch elements that we discussed so far, both the rectangular and the circular, radiate primarily linearly polarized waves if conventional feeds are used with no modifications. However, circular and elliptical polarizations can be obtained using various feed arrangements or slight modifications made to the elements. We will discuss here some of these arrangements.

Circular polarization can be obtained if two orthogonal modes are excited with a 90° time-phase difference between them. This can be accomplished by adjusting the physical dimensions of the patch and using either single, or two or more feeds. There have been some suggestions made and reported in the literature using single patches. For a square patch element, the easiest way to excite ideally circular polarization is to feed the element at two adjacent edges, as shown in Figures 14.31(a,b), to excite the two orthogonal modes; the TM^x_{010} with the feed at one edge and the TM^x_{001} with the feed at the other edge. The quadrature phase difference is obtained by feeding the element with a 90° power divider or 90° hybrid. Examples of arrays of linear elements that generate circular polarization are discussed in [87].

For a circular patch, circular polarization for the TM^z_{110} mode is achieved by using two feeds with proper angular separation. An example is shown in Figure 14.31(c) using two coax feeds separated by 90° which generate fields that are orthogonal to each other under the patch, as well as outside the patch. Also with this two-probe arrangement, each probe is always positioned at a point where the field generated by the other probe exhibits a null; therefore there is very little mutual coupling between the two probes. To achieve circular polarization, it is also required that the two feeds are fed in such a manner that there is 90° time-phase difference between the fields of the two; this is achieved through the use of a 90° hybrid, as shown in Figure 14.31(c). The shorting pin is placed at the center of the patch to ground the patch to the ground plane which is not necessary for circular polarization but is used

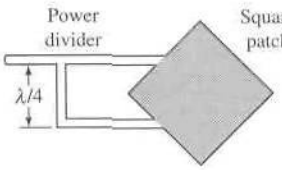

(a) Square patch driven at adjacent sides through a power divider

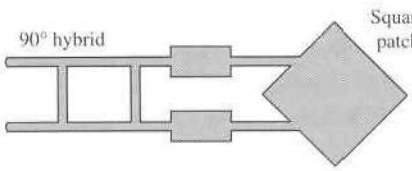

(b) Square patch driven at adjacent sides through a 90° hybrid

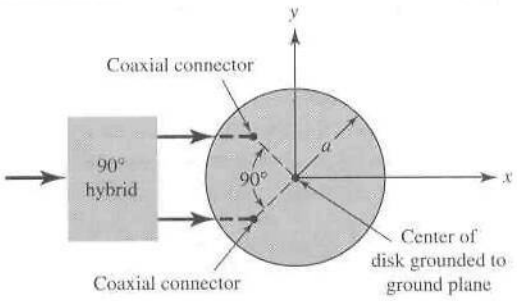

(c) Circular patch fed with coax

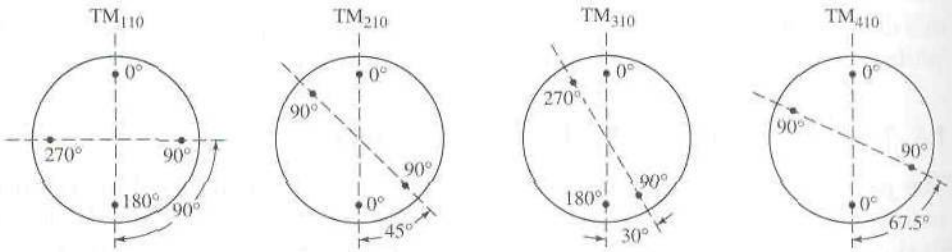

(d) Circular patch feed arrangements for TM^z_{i10} and higher order modes

(Source: J. Huang, "Circularly Polarized Conical Patterns from Circular Microstrip Antennas," IEEE Trans. Antennas Propagat., Vol. AP-32, No. 9, Sept. 1984. © 1984 IEEE.)

Figure 14.31 Rectangular and circular patch arrangements for circular polarization.

to suppress modes with no ϕ variations and also may improve the quality of circular polarization.

For higher order modes, the spacing between the two feeds to achieve circular polarization is different. This is illustrated in Figure 14.31(d) and tabulated in Table 14.1, for the TM^z_{110} [same as in Figure 14.31(c)], TM^z_{210}, TM^z_{310}, and TM^z_{410} modes [88]. However to preserve symmetry and minimize cross polarization, especially for relatively thick substrates, two additional feed probes located diametrically opposite of the original poles are usually recommended. The additional probes are used to suppress the neighboring (adjacent) modes which usually have the next highest magnitudes [88]. For the even modes (TM^z_{210} and TM^z_{410}), the four feed probes should have phases of 0°, 90°, 0° and 90° while the odd modes (TM^z_{110} and TM^z_{310}) should have phases of 0°, 90°, 180° and 270°, as shown in Figure 14.31(d) [88].

To overcome the complexities inherent in dual-feed arrangements, circular polarization can also be achieved with a single feed. One way to accomplish this is to feed the patch at a single point to excite two orthogonal degenerate modes (of some resonant frequency) of ideally equal amplitudes. By introducing then a proper asymmetry in the cavity, the degeneracy can be removed with one mode increasing with

Table 14.1 FEED PROBE ANGULAR SPACING OF DIFFERENT MODES FOR CIRCULAR POLARIZATION (after [88])

	TM_{110}	TM_{210}	TM_{310}	TM_{410}	TM_{510}	TM_{610}
α	90°	45° or 135°	30° or 90°	22.5° or 67.5°	18°, 54° or 90°	15°, 45° or 75°

frequency while the orthogonal mode will be decreasing with frequency by the same amount. Since the two modes will have slightly different frequencies, by proper design the field of one mode can lead by 45° while that of the other can lag by 45° resulting in a 90° phase difference necessary for circular polarization [16]. To achieve this, several arrangements have been suggested.

To illustrate the procedure, let us consider a square patch, as shown in Figure 14.32(a) [34]. Initially assume that the dimensions L and W are nearly the same such that the resonant frequencies of the TM^x_{010} and TM^x_{001} overlap significantly. In the broadside direction to the patch, the TM^x_{010} mode produces an electric far-field E_y which is linearly polarized in the y direction while the TM^x_{001} mode produces an electric far-field E_z which is linearly polarized in the z direction. These fields can be expressed as

$$E_y = c\frac{\sin\left(\frac{\pi}{L}y'\right)}{k^2(1 - j/Q_t) - (k_y)^2} \tag{14-94a}$$

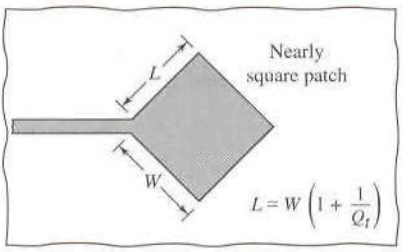

(a) Nearly square patch

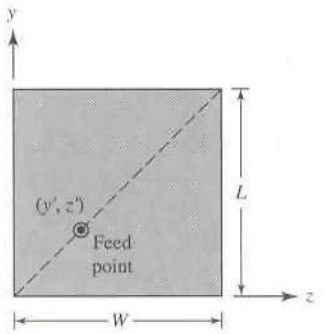

(b) Left-hand circular (LHC)

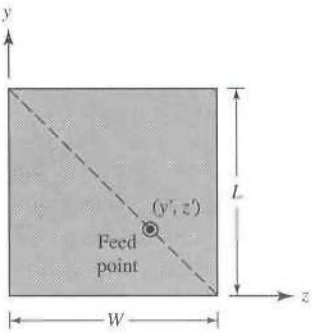

(c) Right-hand circular (RHC)

Figure 14.32 Single-feed arrangements for circular polarization of rectangular microstrip patches.

$$E_z = c\frac{\sin\left(\frac{\pi}{W}z'\right)}{k^2(1 - j/Q_t) - (k_z)^2} \tag{14-94b}$$

$$k_y = \frac{\pi}{L} \tag{14-94c}$$

$$k_z = \frac{\pi}{W} \tag{14-94d}$$

where c (a proportionality constant) and Q_t ($Q_t = 1/\tan \delta_{\text{eff}}$) are identical in the broadside direction for both polarizations. If the feed point (y', z') is selected along the diagonal so that

$$\frac{y'}{L} = \frac{z'}{W} \tag{14-95}$$

then the axial ratio at broadside of the E_y to the E_z field can be expressed as

$$\frac{E_y}{E_z} \simeq \frac{k(1 - j/2Q_t) - k_y}{k(1 - j/2Q_t) - k_z} \tag{14-96}$$

To achieve circular polarization, the magnitude of the axial ratio must be unity while the phase must be $\pm 90°$. This is achieved when the two phasors representing the numerator and denominator are of equal magnitude and 90° out of phase. This can occur when [34]

$$k_y - k_z = \frac{k}{Q_t} \tag{14-97}$$

and the operating frequency is selected at the midpoint between the resonant frequencies of the TM^x_{010} and TM^x_{001} modes. The condition of (14-97) is satisfied when

$$L = W\left(1 + \frac{1}{Q_t}\right) \tag{14-98}$$

Based on (14-98) the resonant frequencies f_1 and f_2 of the bandwidth of (14-88a) associated with the two lengths L and W of a rectangular microstrip are [89]

$$f_1 = \frac{f_0}{\sqrt{1 + 1/Q_t}} \tag{14-99a}$$

$$f_2 = f_0\sqrt{1 + 1/Q_t} \tag{14-99b}$$

where f_0 is the center frequency.

Feeding the element along the diagonal starting at the lower left corner toward the upper right corner, shown dashed in Figure 14.32(b), yields ideally left-hand circular polarization at broadside. Right-hand circular polarization can be achieved by feeding along the opposite diagonal, which starts at the lower right corner and proceeds toward the upper left corner, shown dashed in Figure 14.32(c). Instead of moving the feed point each time to change the modes in order to change the type of circular polarization, varactor diodes can be used to adjust the capacitance and bias, which effectively shifts by electrical means the apparent physical location of the feed point.

This type of a feed to achieve circular polarization at broadside has been shown

experimentally to extend to a larger angular region [18]. However, the bandwidth over which circular polarization is maintained, even at broadside, is very narrow. An empirical formula of the percent bandwidth is [34]

$$\text{BW (percent)} \simeq 12\frac{AR}{Q_t} \tag{14-100}$$

where the axial ratio is specified in dB. The design formulas of (14-98) and (14-100) yield good results for Q values as low as 10. Better designs are achieved for values of Q much greater than 10.

Circular polarization can also be achieved by feeding the element off the main diagonals. This can be accomplished if the dimensions of the rectangular patch are related by

$$L = W\left(1 + \frac{A + \dfrac{1}{A}}{2Q_t}\right) \tag{14-101}$$

where

$$A = \frac{\cos\left(\pi\dfrac{y'}{L}\right)}{\cos\left(\pi\dfrac{z'}{W}\right)} \tag{14-101a}$$

There are some other practical ways of achieving nearly circular polarization. For a square patch, this can be accomplished by cutting very thin slots as shown in Figures 14.33(a,b) with dimensions

$$c = \frac{L}{2.72} = \frac{W}{2.72} \tag{14-102a}$$

$$d = \frac{c}{10} = \frac{L}{27.2} = \frac{W}{27.2} \tag{14-102b}$$

An alternative way is to trim the ends of two opposite corners of a square patch and feed at points 1 or 3, as shown in Figure 14.34(a). Circular polarization can also be

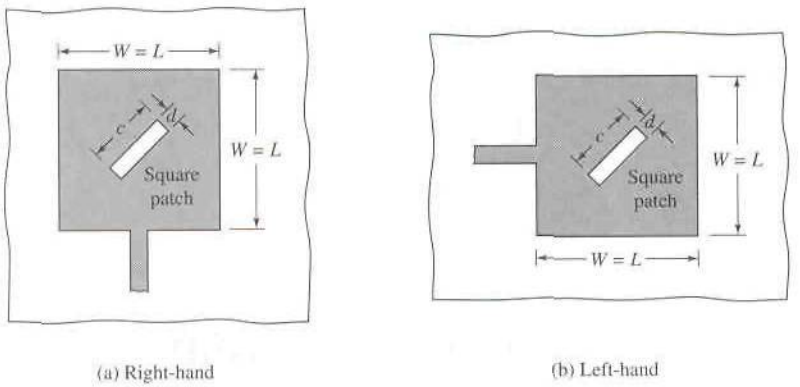

(a) Right-hand (b) Left-hand

Figure 14.33 Circular polarization for square patch with thin slots on patch ($c = W/2.72 = L/2.72$, $d = c/10 = W/27.2 = L/27.2$).

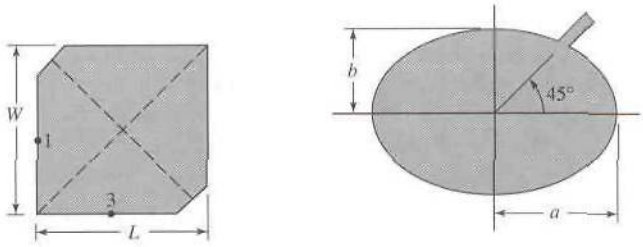

(a) Trimmed square ($L = W$) (b) Elliptical with tabs

Figure 14.34 Circular polarization by trimming opposite corners of a square patch and by making circular-patch slightly elliptical and adding tabs.

achieved with a circular patch by making it slightly elliptical or by adding tabs, as shown in Figure 14.34(b).

Example 14.5

The fractional bandwidth at a center frequency of 10 GHz of a rectangular patch antenna whose substrate is RT/duroid 5880 ($\epsilon_r = 2.2$) with height $h = 0.1588$ cm is about 5% for a VSWR of 2:1. Within that bandwidth, find resonant frequencies associated with the two lengths of the rectangular patch antenna, and the relative ratio of the two lengths.

SOLUTION

The total quality factor Q_t of the patch antenna is found using (14-88a) or

$$Q_t = \frac{1}{0.05\sqrt{2}} = 14.14$$

Using (14-99a) and (14-99b)

$$f_1 = \frac{10 \times 10^9}{\sqrt{1 + 1/14.14}} = 9.664 \text{ GHz}$$

$$f_2 = 10 \times 10^9 \sqrt{1 + 1/14.14} = 10.348 \text{ GHz}$$

The relative ratio of the two lengths according to (14-98) is

$$\frac{L}{W} = 1 + \frac{1}{Q_t} = 1 + \frac{1}{14.14} = 1.07$$

which makes the patch nearly square.

14.8 ARRAYS AND FEED NETWORKS

Microstrip antennas are used not only as single elements but are very popular in arrays [17], [23], [30], [31], [50], [51], [54], [63]–[65], and [74]–[77]. As discussed in

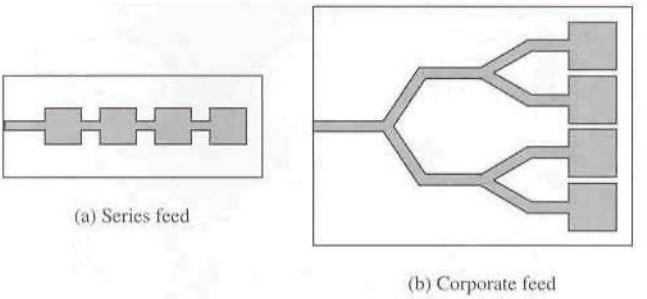

Figure 14.35 Feed arrangements for microstrip patch arrays.

Chapter 6, arrays are very versatile and are used, among other things, to synthesize a required pattern that cannot be achieved with a single element. In addition, they are used to scan the beam of an antenna system, increase the directivity, and perform various other functions which would be difficult with any one single element. The elements can be fed by a single line, as shown in Figure 14.35(a), or by multiple lines in a feed network arrangement, as shown in Figure 14.35(b). The first is referred to as a *series-feed network* while the second is referred to as a *corporate-feed network.*

The corporate-feed network is used to provide power splits of 2^n (i.e., n = 2, 4, 8, 16, 32, etc.). This is accomplished by using either tapered lines, as shown in Figure 14.36(a), to match 100-ohm patch elements to a 50-ohm input or using quarter-wavelength impedance transformers, as shown in Figure 14.36(b) [3]. The design of

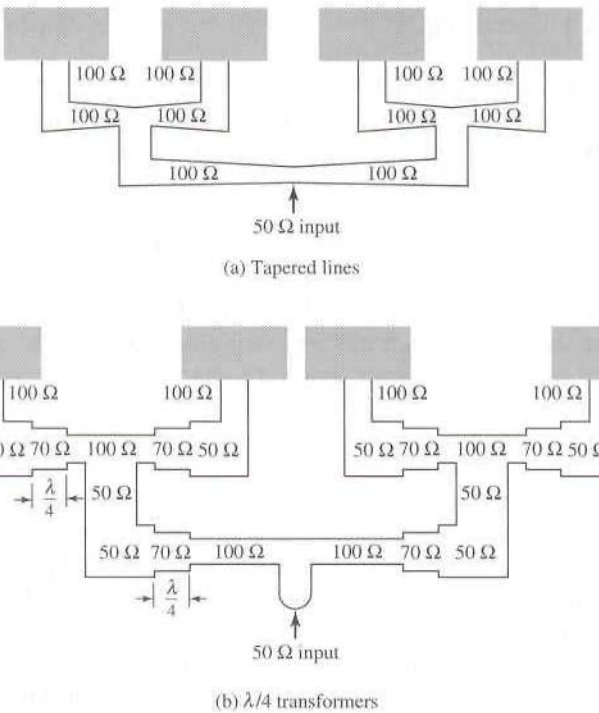

Figure 14.36 Tapered and λ/4 impedance transformer lines to match 100-ohm patches to a 50-ohm line. (SOURCE: R. E. Munson, "Conformal Microstrip Antennas and Microstrip Phased Arrays," *IEEE Trans. Antennas Propagat.*, Vol. AP-22, No. 1, January 1974. © 1974 IEEE)

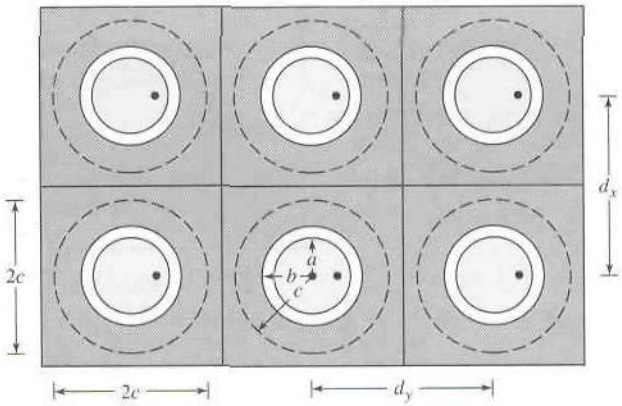

(a) Top view

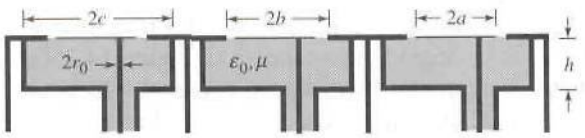

(b) Side view

Figure 14.37 Infinite array of circular patches backed by circular cavities. (Courtesy J. T. Aberle and F. Zavosh)

single- and multiple-section quarter-wavelength impedance transformers is discussed in Section 9.8.

Series-fed arrays can be conveniently fabricated using photolithography for both the radiating elements and the feed network. However, this technique is limited to arrays with a fixed beam or those which are scanned by varying the frequency, but it can be applied to linear and planar arrays with single or dual polarization. Also any changes in one of the elements or feed lines affects the performance of the others. Therefore in a design it is important to be able to take into account these and other effects, such as mutual coupling, and internal reflections.

Corporate-fed arrays are general and versatile. With this method the designer has more control of the feed of each element (amplitude and phase) and it is ideal for scanning phased arrays, multibeam arrays, or shaped-beam arrays. As discussed in Chapter 6, the phase of each element can be controlled using phase shifters while the amplitude can be adjusted using either amplifiers or attenuators.

Those who have been designing and testing microstrip arrays indicate that radiation from the feed line, using either a series or corporate feed network, is a serious problem that limits the cross-polarization and side lobe level of the arrays [38]. Both cross-polarization and side lobe levels can be improved by isolating the feed network from the radiating face of the array. This can be accomplished using either probe feeds or aperture coupling.

Arrays can be analyzed using the theory of Chapter 6. However, such an approach does not take into account mutual coupling effects, which for microstrip patches can be significant. Therefore for more accurate results, full-wave solutions must be performed. In microstrip arrays [63], as in any other array [90], mutual coupling between

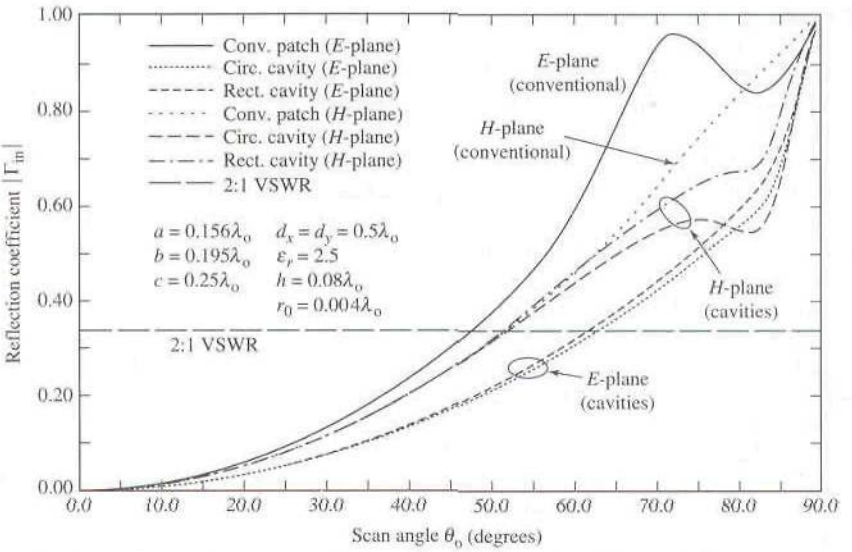

Figure 14.38 *E*- and *H*-plane broadside-matched input reflection coefficient versus scan angle for infinite array of circular microstrip patches with and without cavities. (Courtesy J. T. Aberle and F. Zavosh)

elements can introduce *scan blindness* which limits, for a certain maximum reflection coefficient, the angular volume over which the arrays can be scanned. For microstrip antennas, this scan limitation is strongly influenced by surface waves within the substrate. This scan angular volume can be extended by eliminating surface waves. One way to do this is to use cavities in conjunction with microstrip elements [50], [51]. Figure 14.37 shows an array of circular patches backed by either circular or rectangular cavities. It has been shown that the presence of cavities, either circular or rectangular, can have a pronounced enhancement in the *E*-plane scan volume, especially for thicker substrates [51]. The *H*-plane scan volume is not strongly enhanced. However the shape of the cavity, circular or rectangular, does not strongly influence the results. Typical results for broadside-matched reflection coefficient infinite array of circular patches, with a substrate $0.08\lambda_0$ thick and backed by circular and rectangular cavities, are shown in Figure 14.38 for the *E*-plane and *H*-plane. The broadside-matched reflection coefficient $\Gamma(\theta, \phi)$ is defined as

$$\Gamma(\theta, \phi) = \frac{Z_{in}(\theta, \phi) - Z_{in}(0, 0)}{Z_{in}(\theta, \phi) + Z_{in}^{*}(0, 0)} \tag{14-103}$$

where $Z_{in}(\theta, \phi)$ is the input impedance when the main beam is scanned toward an angle (θ, ϕ). The results are compared with those of a conventional cavity (noncavity backed). It is apparent that there is a significant scan enhancement for the *E*-plane, especially for a VSWR of about 2:1. *H*-plane enhancement occurs for reflection coefficients greater than about 0.60. For the conventional array, the *E*-plane response exhibits a large reflection coefficient, which approaches unity, near a scan angle of $\theta_0 = 72.5°$. This is evidence of scan blindness which ideally occurs when the reflection coefficient is unity, and it is attributed to the coupling between the array elements due to leaky waves [63]. Scan blindness occurs for both the *E*- and *H*-planes at grazing incidence ($\theta_0 = 90°$).

References

1. G. A. Deschamps, "Microstrip Microwave Antennas," presented at the Third USAF Symposium on Antennas, 1953.
2. H. Gutton and G. Baissinot, "Flat Aerial for Ultra High Frequencies," French Patent No. 703 113, 1955.
3. R. E. Munson, "Conformal Microstrip Antennas and Microstrip Phased Arrays," *IEEE Trans. Antennas Propagat.*, Vol. AP-22, No. 1, pp. 74–78, January 1974.
4. J. W. Howell, "Microstrip Antennas," *IEEE Trans. Antennas Propagat.*, Vol. AP-23, No. 1, pp. 90–93, January 1975.
5. A. G. Derneryd, "Linearly Polarized Microstrip Antennas," *IEEE Trans. Antennas Propagat.*, Vol. AP-24, No. 6, pp. 846–851, November 1976.
6. L. C. Shen, S. A. Long, M. R. Allerding, and M. D. Walton, "Resonant Frequency of a Circular Disc, Printed-Circuit Antenna," *IEEE Trans. Antennas Propagat.*, Vol. AP-25, No. 4, pp. 595–596, July 1977.
7. P. K. Agrawal and M. C. Bailey, "An Analysis Technique for Microstrip Antennas," *IEEE Trans. Antennas Propagat.*, Vol. AP-25, No. 6, pp. 756–759, November 1977.
8. A. G. Derneryd, "A Theoretical Investigation of the Rectangular Microstrip Antenna Element," *IEEE Trans. Antennas Propagat.*, Vol. AP-26, No. 4, pp. 532–535, July 1978.
9. *Proc. of the Workshop on Printed-Circuit Antenna Technology*, October 17–19, 1979, New Mexico State Univ., Las Cruces, NM.
10. A. G. Derneryd, "Analysis of the Microstrip Disk Antenna Element," *IEEE Trans. Antennas Propagat.*, Vol. AP-27, No. 5, pp. 660–664, September 1979.
11. A. G. Derneryd, "Extended Analysis of Rectangular Microstrip Resonator Antennas," *IEEE Trans. Antennas Propagat.*, Vol. AP-27, No. 6, pp. 846–849, November 1979.
12. Y. T. Lo, D. Solomon, and W. F. Richards, "Theory and Experiment on Microstrip Antennas," *IEEE Trans. Antennas Propagat.*, Vol. AP-27, No. 2, pp. 137–145, March 1979.
13. S. A. Long and M. D. Walton, "A Dual-Frequency Stacked Circular-Disc Antenna," *IEEE Trans. Antennas Propagat.*, Vol. AP-27, No. 2, pp. 270–273, March 1979.
14. N. K. Uzunoglu, N. G. Alexopoulos, and J. G. Fikioris, "Radiation Properties of Microstrip Dipoles," *IEEE Trans. Antennas Propagat.*, Vol. AP-27, No. 6, pp. 853–858, November 1979.
15. I. J. Bahl and P. Bhartia, *Microstrip Antennas*, Artech House, Dedham, MA, 1980.
16. K. R. Carver and J. W. Mink, "Microstrip Antenna Technology," *IEEE Trans. Antennas Propagat.*, Vol. AP-29, No. 1, pp. 2–24, January 1981.
17. R. J. Mailloux, J. F. McIlvenna, and N. P. Kernweis, "Microstrip Array Technology," *IEEE Trans. Antennas Propagat.*, Vol. AP-29, No. 1, pp. 25–27, January 1981.
18. W. F. Richards, Y. T. Lo, and D. D. Harrison, "An Improved Theory of Microstrip Antennas with Applications," *IEEE Trans. Antennas Propagat.*, Vol. AP-29, No. 1, pp. 38–46, January 1981.
19. E. H. Newman and P. Tylyathan, "Analysis of Microstrip Antennas Using Moment Methods," *IEEE Trans. Antennas Propagat.*, Vol. AP-29, No. 1, pp. 47–53, January 1981.
20. D. C. Chang, "Analytical Theory of an Unloaded Rectangular Microstrip Patch," *IEEE Trans. Antennas Propagat.*, Vol. AP-29, No. 1, pp. 54–62, January 1981.
21. T. Itoh and W. Menzel, "A Full-Wave Analysis Method for Open Microstrip Structures," *IEEE Trans. Antennas Propagat.*, Vol. AP-29, No. 1, pp. 63–68, January 1981.
22. I. E. Rana and N. G. Alexopoulos, "Current Distribution and Input Impedance of Printed Dipoles," *IEEE Trans. Antennas Propagat.*, Vol. AP-29, No. 1, pp. 99–105, January 1981.
23. N. G. Alexopoulos and I. E. Rana, "Mutual Impedance Computation Between Printed Dipoles," *IEEE Trans. Antennas Propagat.*, Vol. AP-29, No. 1, pp. 106–111, January 1981.

24. J. R. James, P. S. Hall, C. Wood, and A. Henderson, "Some Recent Developments in Microstrip Antenna Design," *IEEE Trans. Antennas Propagat.*, Vol. AP-29, No. 1, pp. 124–128, January 1981.
25. M. D. Deshpande and M. C. Bailey, "Input Impedance of Microstrip Antennas," *IEEE Trans. Antennas Propagat.*, Vol. AP-30, No. 4, pp. 645–650, July 1982.
26. M. C. Bailey and M. D. Deshpande, "Integral Equation Formulation of Microstrip Antennas," *IEEE Trans. Antennas Propagat.*, Vol. AP-30, No. 4, pp. 651–656, July 1982.
27. D. M. Pozar, "Input Impedance and Mutual Coupling of Rectangular Microstrip Antenna," *IEEE Trans. Antennas Propagat.*, Vol. AP-30, No. 6, pp. 1191–1196, November 1982.
28. D. M. Pozar, "Considerations for Millimeter-Wave Printed Antennas," *IEEE Trans. Antennas Propagat.*, Vol. AP-31, No. 5, pp. 740–747, September 1983.
29. E. F. Kuester and D. C. Chang, "A Geometrical Theory for the Resonant Frequencies and Q- Factors of Some Triangular Microstrip Patch Antennas," *IEEE Trans. Antennas Propagat.*, Vol. AP-31, No. 1, pp. 27–34, January 1983.
30. P. B. Katehi and N. G. Alexopoulos, "On the Modeling of Electromagnetically Coupled Microstrip Antennas-The Printed Strip Dipole," *IEEE Trans. Antennas Propagat.*, Vol. AP-32, No. 11, pp. 1179–1186, November 1984.
31. D. M. Pozar, "Analysis of Finite Phased Arrays of Printed Dipoles," *IEEE Trans. Antennas Propagat.*, Vol. AP-33, No. 10, pp. 1045–1053, October 1985.
32. J. R. James, P. S. Hall, and C. Wood, *Microstrip Antenna Theory and Design*, Peter Peregrinus, 1981, London, UK, 1981.
33. R. E. Munson, "Microstrip Antennas," Chapter 7 in *Antenna Engineering Handbook* (R. C. Johnson and H. Jasik, eds.), McGraw-Hill Book Co., New York, 1984.
34. W. F. Richards, "Microstrip Antennas," Chapter 10 in *Antenna Handbook: Theory, Applications and Design* (Y. T. Lo and S. W. Lee, eds.), Van Nostrand Reinhold Co., New York, 1988.
35. J. R. James, and P. S. Hall, *Handbook of Microstrip Antennas*, Vols. 1 and 2, Peter Peregrinus, London, UK, 1989.
36. P. Bhartia, K. V. S. Rao, and R. S. Tomar, *Millimeter-Wave Microstrip and Printed Circuit Antennas*, Artech House, Boston, MA, 1991.
37. J. R. James, "What's New in Antennas," *IEEE Antennas and Propagation Magazine*, Vol. 32, No. 1, pp. 6–18, February 1990.
38. D. M. Pozar, "Microstrip Antennas," *Proc. IEEE*, Vol. 80, No. 1, pp. 79–81, January 1992.
39. D. H. Schaubert, F. G. Farrar, A. Sindoris, and S. T. Hayes, "Microstrip Antennas with Frequency Agility and Polarization Diversity," *IEEE Trans. Antennas Propagat.*, Vol. AP-29, No. 1, pp. 118–123, January 1981.
40. P. Bhartia and I. J. Bahl, "Frequency Agile Microstrip Antennas," *Microwave Journal*, pp. 67–70, October 1982.
41. W. F. Richards and Y. T. Lo, "Theoretical and Experimental Investigation of a Microstrip Radiator with Multiple Lumped Linear Loads," *Electromagnetics*, Vol. 3, No. 3–4, pp. 371–385, July–December 1983.
42. W. F. Richards and S. A. Long, "Impedance Control of Microstrip Antennas Utilizing Reactive Loading," *Proc. Intl. Telemetering Conf.*, pp. 285–290, Las Vegas, 1986.
43. W. F. Richards and S. A. Long, "Adaptive Pattern Control of a Reactively Loaded, Dual-Mode Microstrip Antenna," *Proc. Intl. Telemetering Conf.*, pp. 291–296, Las Vegas, 1986.
44. M. P. Purchine and J. T. Aberle, "A Tunable L-Band Circular Microstrip Patch Antenna," *Microwave Journal*, pp. 80, 84, 87, and 88, October 1994.
45. C. M. Krowne, "Cylindrical-Rectangular Microstrip Antenna," *IEEE Trans. Antennas Propagat.*, Vol. AP-31, No. 1, pp. 194–199, January 1983.
46. S. B. De Assis Fonseca and A. J. Giarola, "Microstrip Disk Antennas, Part I: Efficiency of Space Wave Launching," *IEEE Trans. Antennas Propagat.*, Vol. AP-32, No. 6, pp. 561–567, June 1984.

47. S. B. De Assis Fonseca and A. J. Giarola, "Microstrip Disk Antennas, Part II: the Problem of Surface Wave Radiation by Dielectric Truncation," *IEEE Trans. Antennas Propagat.*, Vol. AP-32, No. 6, pp. 568–573, June 1984.
48. J. Huang, "The Finite Ground Plane Effect on the Microstrip Antenna Radiation Patterns," *IEEE Trans. Antennas Propagat.*, Vol. AP-31, No. 7, pp. 649–653, July 1983.
49. I. Lier and K. R. Jakobsen, "Rectangular Microstrip Patch Antennas with Infinite and Finite Ground-Plane Dimensions," *IEEE Trans. Antennas Propagat.*, Vol. AP-31, No. 6, pp. 978–984, November 1983.
50. R. J. Mailloux, "On the Use of Metallized Cavities in Printed Slot Arrays with Dielectric Substrates," *IEEE Trans. Antennas Propagat.*, Vol. AP-35, No. 5, pp. 477–487, May 1987.
51. J. T. Aberle and F. Zavosh, "Analysis of Probe-Fed Circular Microstrip Patches Backed by Circular Cavities," *Electromagnetics*, Vol. 14, pp. 239–258, 1994.
52. A. Henderson, J. R. James, and C. M. Hall, "Bandwidth Extension Techniques in Printed Conformal Antennas," *Military Microwaves*, MM 86, pp. 329–334, 1986.
53. H. F. Pues and A. R. Van de Capelle, "An Impedance Matching Technique for Increasing the Bandwidth of Microstrip Antennas," *IEEE Trans. Antennas Propagat.*, Vol. AP-37, No. 11, pp. 1345–1354, November 1989.
54. J. J. Schuss, J. D. Hanfling, and R. L. Bauer, "Design of Wideband Patch Radiator Phased Arrays," *IEEE Antennas Propagat. Symp. Dig.*, pp. 1220–1223, 1989.
55. C. H. Tsao, Y. M. Hwang, F. Kilburg, and F. Dietrich, "Aperture-Coupled Patch Antennas with Wide-Bandwidth and Dual Polarization Capabilities," *IEEE Antennas Propagat. Symp. Dig.*, pp. 936–939, 1988.
56. A. Ittipiboon, B. Clarke, and M. Cuhaci, "Slot-Coupled Stacked Microstrip Antennas," *IEEE Antennas Propagat. Symp. Dig.*, pp. 1108–1111, 1990.
57. S. Sabban, "A New Broadband Stacked Two-Layer Microstrip Antenna," *IEEE Antennas Propagat. Symp. Dig.*, pp. 63–66, 1983.
58. C. H. Chen, A. Tulintseff, and M. Sorbello, "Broadband Two-Layer Microstrip Antenna," *IEEE Antennas Propagat. Symp. Dig.*, pp. 251–254, 1984.
59. R. W. Lee, K. F. Lee, and J. Bobinchak, "Characteristics of a Two-Layer Electromagnetically Coupled Rectangular Patch Antenna," *Electronic Letters*, Vol. 23, pp. 1070–1072, September 1987.
60. W. F. Richards, S. Davidson, and S. A. Long, "Dual-Band, Reactively Loaded Microstrip Antennas," *IEEE Trans. Antennas Propagat.*, Vol. AP-33, No. 5, pp. 556–561, May 1985.
61. D. M. Pozar and B. Kaufman, "Increasing the Bandwidth of a Microstrip Antenna by Proximity Coupling," *Electronic Letters*, Vol. 23, pp. 368–369, April 1987.
62. N. W. Montgomery, "Triple-Frequency Stacked Microstrip Element," *IEEE Antennas Propagat. Symp. Dig.*, pp. 255–258, Boston, MA, 1984.
63. D. M. Pozar and D. H. Schaubert, "Scan Blindness in Infinite Phased Arrays of Printed Dipoles," *IEEE Trans. Antennas Propagat.*, Vol. AP-32, No. 6, pp. 602–610, June 1984.
64. D. M. Pozar, "Finite Phased Arrays of Rectangular Microstrip Antennas," *IEEE Trans. Antennas Propagat.*, Vol. AP-34, No. 5, pp. 658–665, May 1986.
65. F. Zavosh and J. T. Aberle, "Infinite Phased Arrays of Cavity-Backed Patches," Vol. AP-42, No. 3, pp. 390–398, March 1994.
66. H. G. Oltman and D. A. Huebner, "Electromagnetically Coupled Microstrip Dipoles," *IEEE Trans. Antennas Propagat.*, Vol. AP-29, No. 1, pp. 151–157, January 1981.
67. D. M. Pozar, "A Microstrip Antenna Aperture Coupled to a Microstrip Line," *Electronic Letters*, Vol. 21, pp. 49–50, January 1985.
68. G. Gronau and I. Wolff, "Aperture-Coupling of a Rectangular Microstrip Resonator," *Electronic Letters*, Vol. 22, pp. 554–556, May 1986.
69. H. A. Bethe, "Theory of Diffractions by Small Holes," *Physical Review*, Vol. 66, pp. 163–182, 1944.
70. R. E. Collin, *Foundations for Microwave Engineering*, Chapter 6, McGraw-Hill Book Co., New York, 1992.

71. J. R. Mosig and F. E. Gardiol, "General Integral Equation Formulation for Microstrip Antennas and Scatterers," *Proc. Inst. Elect. Eng.*, pt. H, Vol. 132, pp. 424–432, 1985.
72. N. G. Alexopoulos and D. R. Jackson, "Fundamental Superstrate (Cover) Effects on Printed Circuit Antennas," *IEEE Trans. Antennas Propagat.*, Vol. AP-32, No. 8, pp. 807–816, August 1984.
73. C. C. Liu, A. Hessel, and J. Shmoys, "Performance of Probe-Fed Rectangular Microstrip Patch Element Phased Arrays," *IEEE Trans. Antennas Propagat.*, Vol. AP-36, No. 11, pp. 1501–1509, November 1988.
74. J. T. Aberle and D. M. Pozar, "Analysis of Infinite Arrays of One- and Two-Probe-Fed Circular Patches," *IEEE Trans. Antennas Propagat.*, Vol. AP-38, No. 4, pp. 421–432, April 1990.
75. E. H. Van Lil and A. R. Van de Capelle, "Transmission-Line Model for Mutual Coupling Between Microstrip Antennas," *IEEE Trans. Antennas Propagat.*, Vol. AP-32, No. 8, pp. 816–821, August 1984.
76. K. Malkomes, "Mutual Coupling Between Microstrip Patch Antennas," *Electronic Letters*, Vol. 18, No. 122, pp. 520–522, June 1982.
77. E. Penard and J.-P. Daniel, "Mutual Coupling Between Microstrip Antennas," *Electronic Letters*, Vol. 18, No. 4, pp. 605–607, July 1982.
78. D. H. Schaubert, D. M. Pozar, and A. Adrian, "Effect of Microstrip Antenna Substrate Thickness and Permittivity: Comparison of Theories and Experiment," *IEEE Trans. Antennas Propagat.*, Vol. AP-37, No. 6, pp. 677–682, June 1989.
79. C. A. Balanis, *Advanced Engineering Electromagnetics*, John Wiley & Sons, New York, 1989.
80. E. O. Hammerstad, "Equations for Microstrip Circuit Design," *Proc. Fifth European Microwave Conf.*, pp. 268–272, September 1975.
81. R. F. Harrington, *Time-Harmonic Electromagnetic Fields*, McGraw-Hill Book Co., p. 183, 1961.
82. R. E. Collin and F. J. Zucker, *Antenna Theory*, Part I, Chapter 5, McGraw-Hill Book Co., New York, 1969.
83. E. J. Martin, "Radiation Fields of Circular Loop Antennas by a Direct Integration Process," *IRE Trans. Antennas Propagat.*, Vol. AP-8, pp. 105–107, January 1960.
84. R. J. Collier and P. D. White, "Surface Waves in Microstrip Circuits," *Proc. 6th European Microwave Conference*, 1976, pp. 632–636.
85. W. F. Richards, J. R. Zinecker, R. D. Clark, and S. A. Long, "Experimental and Theoretical Investigation of the Inductance Associated with a Microstrip Antenna Feed," *Electromagnetics*, Vol. 3, No. 3–4, pp. 327–346, July–December 1983.
86. L. B. Felsen and N. Marcuvitz, *Radiation and Scattering of Waves*, Prentice-Hall, Englewood Cliffs, NJ, 1973.
87. J. Huang, "A Technique for an Array to Generate Circular Polarization with Linearly Polarized Elements," *IEEE Trans. Antennas Propagat.*, Vol. AP-34, No. 9, pp. 1113–1124, September 1986.
88. J. Huang, "Circularly Polarized Conical Patterns from Circular Microstrip Antennas," *IEEE Trans. Antennas Propagat.*, Vol. AP-32, No. 9, pp. 991–994, September 1984.
89. T. A. Milligan, *Modern Antenna Design*, McGraw-Hill Book Co., New York, 1985.
90. R. J. Mailloux, "Phase Array Theory and Technology," *Proc. IEEE*, Vol. 70, No. 3, pp. 246–291, March 1982.

PROBLEMS

14.1. A microstrip line is used as a feed line to a microstrip patch. The substrate of the line is alumina ($\epsilon_r \simeq 10$) while the dimensions of the line are $w/h = 1.2$ and $t/h = 0$. Determine the effective dielectric constant and characteristic impedance of the line. Compare the computed characteristic impedance to that of a 50-ohm line.

14.2. A microstrip transmission line of beryllium oxide ($\epsilon_r \simeq 6.8$) has a width-to-height ratio of $w/h = 1.5$. Assuming that the thickness-to-height ratio is $t/h = 0$, determine:

(a) effective dielectric constant
(b) characteristic impedance of the line

14.3. Cellular and mobile telephony, using earth-based repeaters, has received wide acceptance and has become an essential means of communication for business, even for the household. Cellular telephony by satellites is the wave of the future and communication systems are being designed for that purpose. The present allocated frequency band for satellites is at L-band ($\simeq$ 1.6 GHz). Various antennas are being examined for that purpose; one candidate is the microstrip patch antenna. Design a rectangular microstrip patch antenna, based on the dominant mode, that can be mounted on the roof of a car to be used for satellite cellular telephone. The designed center frequency is 1.6 GHz, the dielectric constant of the substrate is 10.2 (i.e., RT/duroid), and the thickness of the substrate is 0.127 cm. Determine the
(a) dimensions of the rectangular patch (in cm)
(b) resonant input impedance, assuming no coupling between the two radiating slots
(c) mutual conductance between the two radiating slots of the patch
(d) resonant input impedance, taking into account coupling
(e) position of the feed to match the antenna patch to a 75-ohm line

14.4. Repeat the design of Problem 14.3 using a substrate with a dielectric constant of 2.2 (i.e., RT/duroid 5880) and with a height of 0.1575 cm. Are the new dimensions of the patch realistic for the roof of a personal car?

14.5. Design a rectangular microstrip patch with dimensions W and L, over a single substrate, whose center frequency is 10 GHz. The dielectric constant of the substrate is 10.2 and the height of the substrate is 0.127 cm (0.050 in.). Determine the physical dimensions W and L (in cm) of the patch, taking into account field fringing.

14.6. Using the transmission line model of Figure 14.8(b), derive (14-14)–(14-15).

14.7. To take into account coupling between the two radiating slots of a rectangular microstrip patch, the resonant input resistance is represented by (14-17). Justify, explain, and/or show why the plus (+) sign is used for modes with odd (antisymmetric) resonant voltage distribution beneath the patch while the minus (−) sign is used for modes with even (symmetric) resonant voltage distribution.

14.8. Show that for typical rectangular microstrip patches $G_1/Y_c \ll 1$ and $B_1/Y_c \ll 1$ so that (14-20) reduces to (14-20a).

14.9. A rectangular microstrip patch antenna operating at 10 GHz with a substrate with dimensions of length $L = 0.4097$ cm, width $W = 0.634$ cm, and substrate height $h = 0.127$ cm. It is desired to feed the patch using a probe feed. Neglecting mutual coupling, calculate:
(a) What is the input impedance of the patch at one of the radiating edges based on the transmission-line model?
(b) At what distance y_0 (in cm) from one of the radiating edges should the coax feed be placed so that the input impedance is 50 ohms?

14.10. A rectangular microstrip patch antenna, whose input impedance is 152.44 ohms at its leading radiating edge, is fed by a microstrip line as shown in Figure 14.10. Assuming the width of the feeding line is $W_0 = 0.2984$ cm, the height of the substrate is 0.1575 cm and the dielectric constant of the substrate is 2.2, at what distance y_0 should the microstrip patch antenna be fed so as to have a perfect match between the line and the radiating element? The overall microstrip patch element length is 0.9068 cm.

14.11. The rectangular microstrip patch of Example 14.2 is fed by a microstrip transmission line of Figure 14.5. In order to reduce reflections at the inset feed point between the line and the patch element, design the microstrip line that its characteristic impedance matches that of the radiating element.

14.12. Repeat the design of Example 14.2 so that the input impedance of the radiating patch at the feed point is:
(a) 75 ohms
(b) 100 ohms

Then, assuming the feed line is a microstrip line, determine the dimensions of the line so that its characteristic impedance matches that of the radiating patch.

14.13. A rectangular microstrip patch antenna has dimensions of $L = 0.906$ cm, $W = 1.186$ cm, and $h = 0.1575$ cm. The dielectric constant of the substrate is $\epsilon_r = 2.2$. Using the geometry of Figure 14.12 and assuming no fringing, determine the resonant frequency of the first 4 TM^z_{0np} modes, in order of ascending resonant frequency.

14.14. Derive the TM^z_{mnp} field configurations (modes) for the rectangular microstrip patch based on the geometry of Figure P14.14. Determine the:
(a) eigenvalues
(b) resonant frequency $(f_r)_{mnp}$ for the mnp mode.
(c) dominant mode if $L > W > h$
(d) resonant frequency of the dominant mode.

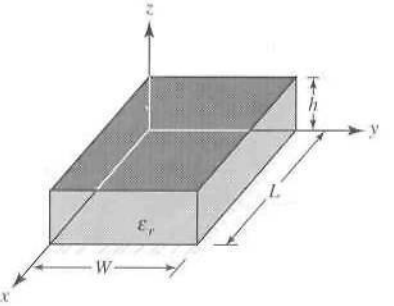

14.15. Repeat Problem 14.14 for the TM^y_{mnp} modes based on the geometry of Figure P14.15.

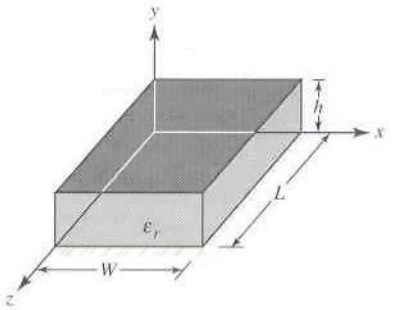

14.16. Derive the array factor of (14-42).

14.17. Assuming the coordinate system for the rectangular microstrip patch is that of Problem 14.14 (Fig. P14.14), derive based on the cavity model the
(a) far-zone electric field radiated by one of the radiating slots of the patch
(b) array factor for the two radiating slots of the patch
(c) far-zone total electric field radiated by both of the radiating slots

14.18. Repeat Problem 14.17 for the rectangular patch geometry of Problem 14.15 (Fig. P14.15).

14.19. Determine the directivity (in dB) of the rectangular microstrip patch of Example 14.3 using
(a) Kraus' approximate formula
(b) Tai & Pereira's approximate formula

14.20. Derive the directivity (in dB) of the rectangular microstrip patch of Problem 14.3.

14.21. Derive the directivity (in dB) of the rectangular microstrip patch of Problem 14.4.

14.22. For a circular microstrip patch antenna operating in the dominant TM^z_{110} mode, derive the far-zone electric fields radiated by the patch based on the cavity model.

14.23. Using the cavity model, derive the TM^z_{mnp} resonant frequencies for a microstrip patch whose shape is that of a half of a circular patch (semicircle).

14.24. Repeat Problem 14.23 for a 90° circular disc (angular sector of 90°) microstrip patch.

14.25. Repeat Problem 14.23 for the circular sector microstrip patch antenna whose geometry is shown in Figure P14.25.

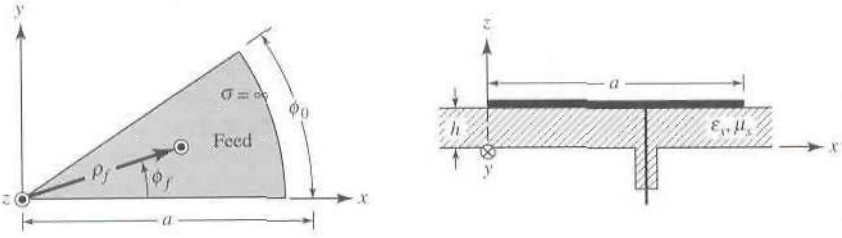

14.26. Repeat Problem 14.23 for the annular microstrip patch antenna whose geometry is shown in Figure P14.26.

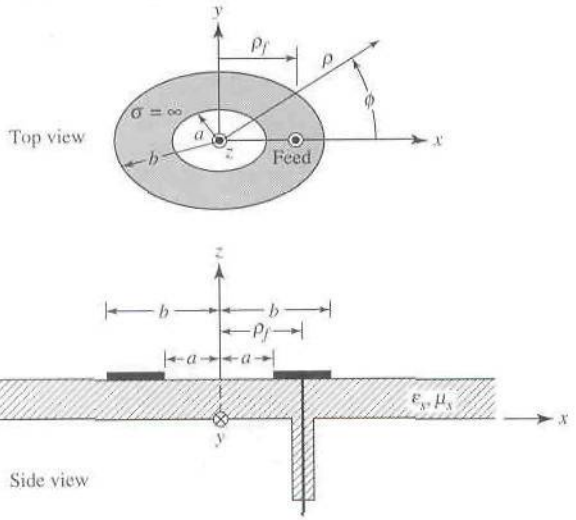

14.27. Repeat Problem 14.23 for the annular sector microstrip patch antenna whose geometry is shown in Figure P14.27.

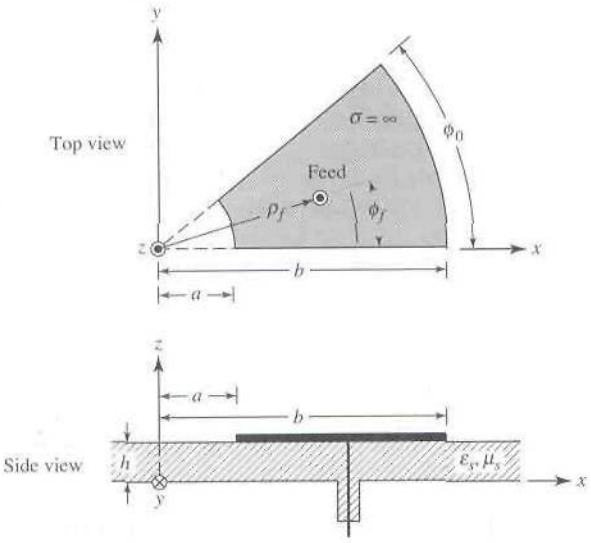

14.28. Repeat the design of Problem 14.3 for a circular microstrip patch antenna operating in the dominant TM^{z}_{110} mode.

14.29. Repeat the design of Problem 14.4 for a circular microstrip patch antenna operating in the dominant TM^{z}_{110} mode.

14.30. For ground-based cellular telephony, the desired pattern coverage is omnidirectional and similar to that of a monopole (with a null toward zenith). This can be accomplished using circular microstrip patch antennas operating in higher order modes, such as the TM^{z}_{210}, TM^{z}_{310}, TM^{z}_{410}, etc. Assuming that the desired resonant frequency is 900 MHz, design a circular microstrip patch antenna operating in the TM^{z}_{210} mode. Assuming a substrate with a dielectric constant of 10.2 and a height of 0.127 cm:
(a) Derive an expression for the resonant frequency.
(b) Determine the radius of the circular patch. Neglect fringing.
(c) Derive expressions for the far-zone radiated fields.
(d) Plot the normalized E- and H-plane amplitude patterns (in dB).
(e) Plot the normalized azimuthal (xy plane) amplitude pattern (in dB).
(f) Determine the directivity (in dB) using the DIRECTIVITY computer program at the end of Chapter 2.

14.31. Repeat Problem 14.30 for the TM^{z}_{310} mode.

14.32. Repeat Problem 14.30 for the TM^{z}_{410} mode.

14.33. The diameter of a typical probe feed for a microstrip patch antenna is $d = 0.1$ cm. At $f = 10$ GHz, determine the feed reactance assuming a substrate with a dielectric constant of 2.2 and height of 0.1575 cm.

14.34. Determine the impedance of a single-section quarter-wavelength impedance transformer to match a 100-ohm patch element to a 50-ohm microstrip line. Determine the dimensions of the line assuming a substrate with a dielectric constant of 2.2 and a height of 0.1575 cm.

14.35. Repeat the design of Problem 14.34 using a two-section binomial transformer. Determine the dimensions of each section of the transformer.

14.36. Repeat the design of Problem 14.34 using a two-section Tschebyscheff transformer. Determine the dimensions of each section of the transformer.